Visual physiology of the Layer 4 cortical circuit *in silico*

Anton Arkhipov[1]*, Nathan W. Gouwens[1], Yazan N. Billeh[1], Sergey Gratiy[1], Ramakrishnan Iyer[1],

Ziqiang Wei[2], Zihao Xu[3], Jim Berg[1], Michael Buice[1], Nicholas Cain[1], Nuno da Costa[1], Saskia de

Vries[1], Daniel Denman[1], Severine Durand[1], David Feng[1], Tim Jarsky[1], Jerome Lecoq[1], Brian Lee[1],

Lu Li[1], Stefan Mihalas[1], Gabriel K. Ocker[1], Shawn R. Olsen[1], R. Clay Reid[1], Gilberto Soler-Llavina[4],

Staci A. Sorensen[1], Quanxin Wang[1], Jack Waters[1], Massimo Scanziani[5], Christof Koch[1]

Affiliations

[1] Allen Institute for Brain Science, Seattle, Washington 98109, USA

[2] Janelia Research Campus, Howard Hughes Medical Institute, Ashburn, Virginia 20147, USA

[3] University of California San Diego, La Jolla, CA 92093, USA

[4] Novartis Institutes for BioMedical Research, Cambridge, MA 02139, USA

[5] Howard Hughes Medical Institute and Department of Physiology, University of California San Francisco, San Francisco, California 94143, USA.

* Corresponding author: antona@alleninstitute.org.

ABSTRACT

Despite advances in experimental techniques and accumulation of large datasets concerning the composition and properties of the cortex, quantitative modeling of cortical circuits under in-vivo-like conditions remains challenging. Here we report and publicly release a biophysically detailed circuit model of layer 4 in the mouse primary visual cortex, receiving thalamo-cortical visual inputs. The 45,000-neuron model was subjected to a battery of visual stimuli, and results were compared to published work and new in vivo experiments. Simulations reproduced a variety of observations, including effects of optogenetic perturbations. Critical to the agreement between responses in silico and in vivo were the rules of functional synaptic connectivity between neurons. Interestingly, after extreme simplification the model still performed satisfactorily on many measurements, although quantitative agreement with experiments suffered. These results emphasize the importance of functional rules of cortical wiring and enable a next generation of data-driven models of in vivo neural activity and computations.

AUTHOR SUMMARY

How can we capture the incredible complexity of brain circuits in quantitative models, and what can such models teach us about mechanisms underlying brain activity? To answer these questions, we set out to build extensive, bio-realistic models of brain circuitry employing systematic datasets on brain structure and function. Here we report the first modeling results of this project, focusing on the layer 4 of the primary visual cortex (V1) of the mouse. Our simulations reproduced a variety of experimental observations in a large battery of visual stimuli. The results elucidated circuit mechanisms determining patters of neuronal activity in layer 4 – in particular, the roles of feedforward thalamic inputs and specific patterns of intracortical connectivity in producing tuning of neuronal responses to the orientation of motion. Simplification of neuronal models led to specific deficiencies in reproducing experimental data, giving insights into how biological details contribute to various aspects of brain activity. To enable future development of more sophisticated models, we make the software code, the model, and simulation results publicly available.

47

INTRODUCTION

49   Although our knowledge of the cortex has been improving dramatically thanks to the ongoing revolution
50   in experimental neuroscience methods, the field is still far from an overall understanding of cortical
51   circuits and their specific function. One essential component necessary to address this problem is the
52   development of data-driven quantitative models that integrate experimental information and enable
53   predictive simulations under a wide range of realistic *in-vivo*-like conditions – following the dictum
54   attributed to Richard Feynman, "What I cannot create, I do not understand" [1]. Whereas detailed data-
55   driven models of cortical tissue have been reported (e.g., [2]; see also [3]), modeling applications to an
56   *in-vivo*-like regime have been limited (although see, e.g., [4] and references therein).

57   A typical systems neuroscience experiment involves a battery of different stimuli and, ideally,
58   perturbations of the investigated circuit. Reproducing this in simulations of a data-constrained cortical
59   model has proven challenging. To investigate the feasibility of *in-vivo*-like comprehensive simulations,
60   and to build a platform for further studies, we set out to simulate a set of visual physiology experiments
61   in the mouse primary visual cortex (area V1), with the emphasis on the first step in the cortical
62   processing of visual information – namely, modeling the V1 input layer, the layer 4 (L4). We decided
63   early on to replicate a small set of what we consider to be canonical physiological findings characterizing
64   cells in L4 of V1. Given the thousands or more of published experiments carried out over the years in
65   this region of cortex, our list is small, non-exclusive and may be considered idiosyncratic by some.
66   However, we believe it is critical to start somewhere solid before generalizing indiscriminately. Our list
67   of explored phenomena includes the approximately log-normal distributions of firing rates [5],
68   orientation selectivity [6, 7, 8, 9], oscillatory population dynamics [10, 11, 12, 13, 14, 15], sparsity of
69   responses to natural stimuli [16], amplification of thalamic inputs by recurrent connections [17, 18, 19,
70   20, 21, 22, 23], preferential connectivity among similarly tuned neurons [24, 25, 26, 27, 28, 29], and a
71   number of others.

72   The model was constructed in a data-driven fashion from what is known about the L4 circuit
73   organization. Although the model was biophysically detailed, we also used simplifications whenever
74   possible, typically choosing computationally inexpensive approximations for biological mechanisms. A
75   crucial component was a set of filters that represented visual information processing from image to the
76   output of the lateral geniculate nucleus (LGN) of the thalamus, which projects to L4. This feature
77   enabled one to use arbitrary movies as visual stimuli. We presented the same or similar sets of stimuli
78   to the model and to mice in experiments and then compared the *in silico* and *in vivo* responses.

79   We asked three major questions: (1) How well does our model reproduce experimentally observed
80   neural responses from the above list? (2) What are the major mechanisms that determine the neuronal
81   activity patterns? And (3), how does the ability to reproduce experimental recordings depend on the
82   level of granularity of the model?

83   To address (1), we assessed neuronal responses to artificial (e.g., drifting gratings) and naturalistic (e.g.,
84   movies) stimuli and selected a number of features of these responses that are generally considered
85   important and interesting in the field. We then benchmarked the model performance on these features
86   against the experimental data. Whereas typically models are developed to explain a specific
87   phenomenon and may aim to reproduce 1-2 observed quantities, the key element in our study was to

88 observe generalization over a wide variety of visual stimuli and response features. We found that our
89 simulations reproduced many of experimental observations (with some exceptions) under a range of
90 different stimuli.

91 For (2), we performed *in silico* experiments to investigate how individual neurons process inputs from
92 different sources and how recurrent connections shape the network activity. This approach relied in
93 part on simulated optogenetic experiments paralleling *in vivo* optogenetic studies. The most striking
94 observation was that tuning properties of neurons were critically affected by the functional connectivity
95 rules.

96 For question (3), we introduced two much simplified versions of our model, where biophysical neuron
97 models were replaced by point-neuron models with either instantaneous or time-dependent course of
98 synaptic action, and compared simulations of these simplified networks with the biophysical case. We
99 found that, although the simplified network models qualitatively reproduced the trends observed in the
100 biophysical simulations, the quantitative agreement with experiment suffered. The time-dependent
101 synaptic kinetics in the simplified model allowed for better agreement with the biophysical model and
102 experiment, such as, for example, in terms of producing oscillations in a gamma range.

103 No circuit in the brain exists in isolation, but including all the brain complexity in the model is impossible
104 at present due to absence of data and inadequate computing resources. Therefore, we attempted to
105 build a model of L4 of V1, which can be handled with available resources and for which a substantial
106 amount of information could be found. The good performance of the model compared to the
107 experiment may indicate a relative compartmentalization of L4 computation (see Discussion); this
108 should not be expected everywhere in the cortex. Our L4 model provides a comprehensive
109 characterization of activity and mechanisms in this cortical circuit and may serve as a stepping-stone for
110 future, more sophisticated studies of all cortical layers. To enable this, we make the software code, the
111 model, and simulation results publicly available (see SI).

112

113

114 **RESULTS**

115 **Construction and optimization of the model**

116 The network (**Fig. 1a, b**) consisted (see Methods) of models of individual neurons [30] from an early
117 version of the Allen Cell Types Database [31], employing compartmental representation of somato-
118 dendritic morphologies (~100-200 compartments per cell) and 10 active conductances at the soma that
119 enabled spiking and spike adaptation. Although recent additions to the Allen Cell Types Database
120 include models of neurons with active conductances in the dendrites as well, those models are very
121 computationally expensive, which was prohibitive for the breadth of our study (see below). In addition,
122 in terms of somatic spike output, the current versions of such models do not exhibit much better
123 performance than the models with active conductances restricted to the soma [31], and, thus, we used
124 these latter, cheaper models. The cells were distributed uniformly in a cylinder ~400 μm in radius,
125 representing the central portion of V1, and 100 μm height with density of 200,000 mm^{-3} [32]. Five single
126 neuron models represent five "types" of neurons – three major excitatory groups as determined by Cre-
127 lines (Scnn1a, Rorb, Nr5a1, 85% of all cells) and two groups of parvalbumin-positive fast-spiking

128 interneurons (15%, denoted as PV1 and PV2), which form the majority of interneurons in L4 [33]. All
129 10,000 biophysical cells were exact copies of these five models. The cell models correspond to regular-
130 spiking excitatory cells and fast-spiking interneurons (PV+); whereas non-PV+ interneurons do exist in
131 L4, they are a relative minority [33], and therefore were neglected for simplicity. Furthermore, 35,000
132 much simpler leaky-integrate-and-fire (LIF) neurons, with only two groups – excitatory and inhibitory –
133 were placed around the biophysically detailed "core" to prevent boundary artefacts (see SI). The
134 complete model accounted for over half of V1 L4 cells (45,000 out of ~70,000). Below, we primarily
135 focus on the properties of the biophysical core circuit.

136 Three independent instantiations were generated using different random seeds. The connectivity and
137 inputs into these three model instantiations were distinct, but all followed the rules described below.
138 All simulations were performed using the python 2.7 code (an early version of the BioNet package [35])
139 employing NEURON 7.4 [34].

140 Recurrent connections (**Fig. 1c**) were established randomly according to probability decaying with
141 intersomatic distance (e.g., [36]). Recent experiments [25, 26, 27, 29] showed that excitatory neurons in
142 the mouse V1 L2/3 exhibit more likely and stronger connections if neurons prefer similar stimuli ("like-
143 to-like connectivity"). We sought to investigate how such a rule affects neural activity. The rule (**Fig. 1d**)
144 was applied to all excitatory cells by assigning a preferred orientation to each excitatory neuron (which
145 was also used to select LGN inputs, see below) and using the difference between such orientations to
146 compute a probability of connection. A similar like-to-like rule was applied to the amplitude of synaptic
147 weights (**Fig. 1e**). The like-to-like rules were parameterized to correspond approximately to the
148 observations for L2/3 [25] (**Fig. 1f**) and did not apply to pairs containing one or more inhibitory neurons.
149 See Methods for further details.

150 We directly converted visual stimuli to spikes of LGN cells (which provide the input to L4) via linear
151 space-time separable filters (**Fig. 1g**; [37, 38]) of ON, OFF, and ON/OFF types (see Methods), all of which
152 produced relatively transient responses. Such a considerable simplification of the wide variety of
153 response types that the LGN cells exhibit (see, e.g., [17]) was necessary to make the model tractable,
154 especially because rules of connectivity from various functional LGN cell types and L4 in the mouse are
155 largely unknown. Because the retinotopy of the complete model did not cover the entire field of view,
156 we employed 9,000 LGN filters – approximately half of the mouse LGN. Based on the experimental data
157 about receptive fields of L4 neurons [17, 32], we used retinotopy of L4 cells to "pool" inputs from LGN
158 filters with similar retinotopy, and the assigned preferred orientation (see above) to establish the
159 geometry of the ON and OFF subfields (**Fig. 1g**; see Methods, **Fig. 7**). This helped to establish orientation
160 selectivity in the combined LGN inputs to individual L4 cells [32]. Interestingly, we found that in our
161 model the L4 cells that were connected to each other had a higher chance to receive inputs from the
162 same LGN cells, in comparison with unconnected L4 cells (see Methods, **Fig. 7d**). This is consistent with
163 recent experimental observations for L4 and L2/3 cells [27].

164 The numbers of synapses for recurrent connections were chosen based on the literature (see Methods).
165 Using electron microscopy (EM), we found (**Fig. 1h**) that LGN synapses constitute 15-30% of all synapses
166 in the neuropil in L4 (see Methods for details), consistent with observations for mouse S1 and M1 [39].
167 This corresponds to over 1,000 synapses from the LGN per excitatory L4 neuron (given ~8,000 synapses
168 total per mouse V1 cell [32] on average, we assume relatively small L4 neurons to receive ~6,000
169 synapses). Thus, the number of LGN-to-L4 synapses is an order of magnitude higher in the mouse than

5

170   in the cat V1 (for which this number has been long established to be ~100 [40]). These new data
171   determined the numbers of LGN-to-L4 synapses in the model (see Methods for further details). For
172   majority of connections, multiple synapses per connection were assigned, typically in the 3-7 range (see
173   Methods). Synaptic dynamics was described by a sum of two decaying exponentials. We assumed no
174   short-term plasticity as it is plausible that *in vivo* synapses operate at steady-state conditions [18]. Long-
175   term plasticity was neglected because simulations covered several seconds at most.
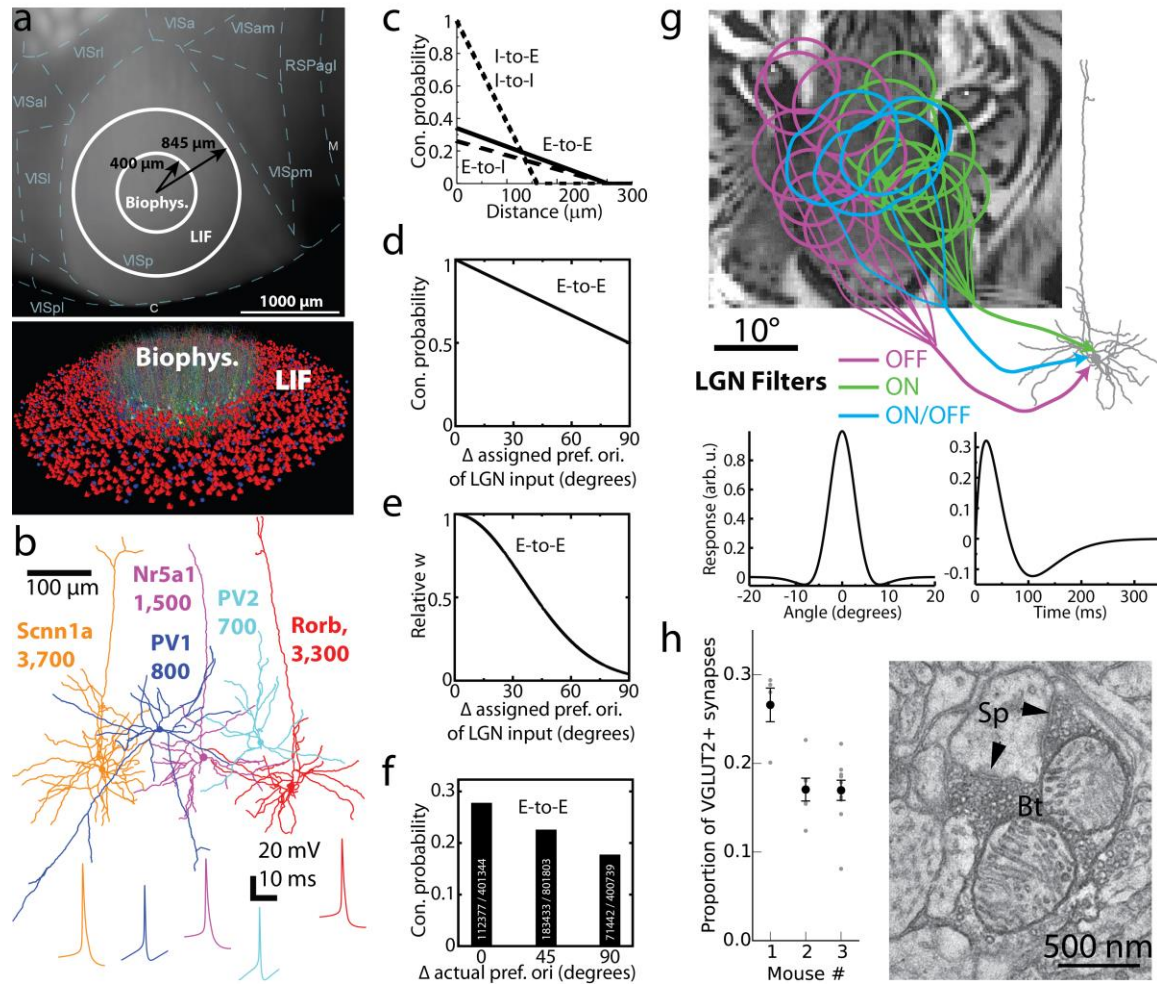
176

177

178

Figure 1. Construction of the model. (a) The biophysical and LIF portions of the model on the cortical surface with delineations of cortical areas (top; "VISp" is V1; the other labels starting with "VIS" correspond to higher visual areas) and with individual cells rendered (bottom; only a small subset of cells is shown for clarity). (b) Morphologies and action potential shapes of the five neuron models used to generate the L4 network; numbers of cells of each type are listed. (c-e) Connection probability (c,d) and synaptic weights (e) of excitatory (E) or inhibitory (I) cell targets and sources. The rules incorporate the dependence on the distance between somata (c) or difference of the assigned preferred orientations, Δori (d, e). Rules dependent on Δori were applied to E-to-E connections only, and synaptic weights for all connections were independent of distance. (f) Connection probability computed for cells within 50 μm using actual preferred orientation observed in simulations (cf. [24]). Numbers of connected and total pairs, used to obtain the probability, are shown inside the bars. (g) Three types of LGN filters (ON, OFF, and ON/OFF), superimposed onto an image, providing inputs to a L4 cell. Example filter's spatial and temporal profiles are at the bottom. (h) The proportion of excitatory thalamocortical synapses (VGLUT2^{+}) in the neuropil of V1 L4, as determined experimentally using EM. Proportions for individual samples of tissue are in gray; mean and s.e.m. for each mouse are in black. Right, an exemplar EM image of a putative VGLUT2+ synapse from the LGN onto an L4 neuron (Sp, spine; Bt, bouton; arrows: postsynaptic densities within the spine).

196

197 To account for inputs from the rest of the brain and for different brain states, we introduced externally
198 generated waves of background activity sweeping across the L4 model (**Fig. 2a**), inspired by reports of
199 activity propagation over cortical surface *in vivo* [41]. Poisson spike generators were distributed within
200 the cortical plane and were activated whenever the wave swept through their positions, sending spikes
201 to the nearby L4 cells. This enabled the L4 model (**Fig. 2b**) to operate with an extremely simple analogue
202 of distinct cortical states (see, e.g., [42, 43, 44]), which we call "Bkg. on" and "Bkg. off." (see Methods).
203 The random generation of the background waves, as well as random generation of background spike
204 trains from the wave profiles and of LGN spike trains from deterministic filter outputs were the sole
205 sources of indeterminacy, leading to differences between individual trials.

206 After the steps above, all parameters were fixed except the synaptic weights (conductance amplitudes).
207 The LGN-to-L4 weights were selected to produce experimentally observed excitatory currents from LGN
208 [17]. The weights for recurrent connections were then manually optimized, while constraining post-
209 synaptic potentials and currents (PSPs and PSCs) to the experimentally reported range for mouse cortex
210 [45] (see Methods). Optimization was limited to two training stimuli – a single trial of a drifting grating
211 and one of a gray screen, 500 ms each. The target was to reproduce the mean spontaneous firing rate
212 and the rate in response to the preferred grating (R_{max}), while avoiding synchronous epileptic-like
213 activity. Published data from [N6] were used for this optimization, before our own experiments were
214 finalized. After optimizing the synaptic weights using this limited training set, we applied the model
215 without any further modification to all the other stimuli, which served as a test set. The exact synaptic
216 weights obtained during the optimization stage may not represent a unique solution, due to degeneracy
217 [46]. Nevertheless, it is reassuring that synaptic properties from our optimized models were consistent
218 with published experimental reports (see **Fig. S2**), exhibiting, e.g., current amplitudes of ~10-30 pA for
219 excitatory and ~40-60 pA for inhibitory synapses [45] or voltage amplitudes of ~1 mV [47] for L4
220 excitatory-to-excitatory connections (as measured at the soma).

221

222 **Benchmarking simulated neuronal activity to the experimental data**

223 How well does the model reproduce experimentally observed neural responses *in vivo*? The answer will
224 depend on the types of stimuli and features of responses to those stimuli that one chooses for
225 comparison. We reasoned that a successful model should be versatile; in other words, it is not sufficient
226 to be able to model responses to one type of stimuli well, and instead one should strive to reproduce
227 features across many types of stimuli. Therefore, our battery of visual stimuli included gray screen, a
228 variety of drifting gratings, 10 natural images, 3 natural movie clips, 2 types of full-field flashes, and 4
229 moving-bar stimuli (see example responses in **Fig. 2c-e**; see also Methods, **Fig. S3**, and **Table S2**).
230 Altogether, ~3,600 simulations were carried out. Our own experiments used for benchmarking
231 consisted of two series of extracellular electrophysiological recordings in mouse V1 employing multi-
232 electrode silicon probes. In the first [7], responses to drifting gratings with a variety of spatial and
233 temporal frequencies were measured, in both awake and anesthetized mice. In the second (previously
234 unpublished), spontaneous activity (responses during gray screen presentation) as well as responses to
235 natural movies, natural images, full-filed flashes, and other stimuli were recorded in awake mice.

236

237 We chose several features of visual responses that are generally considered important and are often
238 reported in the field of cortical visual physiology and compared their values between experiment and
239 simulations (**Fig. 3**). It should be noted that, although the measured metrics differed slightly among the
240 three excitatory cell types (Scnn1a, Rorb, and Nr5a1), as well as among the two inhibitory types (PV1
241 and PV2), we do not ascribe significance to these differences. This is because during model construction
242 and optimization no experimental data was available on distinctions in response features or connectivity
243 between these L4 cell populations, and, in absence of either, we assumed the same optimization targets
244 for all excitatory or inhibitory cells (which, however, allowed for ~1 Hz rate deviation from the target,
245 resulting in different types settling at slightly different activity levels).

246 The first characteristic we checked is whether neuron firing rates follow a positively-skewed, log-normal-
247 like distribution, which is a ubiquitous hallmark feature of brain activity *in vivo* [5]. Such distributions
248 were indeed observed in our simulations for spontaneous activity and all types of visually-driven
249 responses (**Fig. 3a, S5a**). Consistent with published reports, our simulated rate distributions spanned 2-
250 3 decades and may widen further in longer simulations (for instance, spontaneous rates were computed
251 from 20 trials of 500 ms each, resulting in the lowest possible rate of 0.1 Hz). Also in agreement with
252 literature [5], individual neurons tended to keep their low or high firing rates across different stimulus
253 conditions (**Fig. 3a**, top). The positive skewness of firing rate distribution (i.e., the third standardized
254 moment, $\langle \left((f - \langle f \rangle)/\sigma_f \right)^3 \rangle$, where f is the firing rate and σ_f is its standard deviation, both computed
255 in the linear (i.e., not log) firing-rate space) was typically between 0 and 4 (**Fig. S5a**). While it is hard to
256 expect an exact match of the experimental skewness distributions from our relatively rough model, it is
257 reassuring that the model reproduced the overall experimental trends of firing rate distributions with
258 positive skewness in the 0-4 range. Note that a normal distribution has zero skewness, whereas log-
259 normal distribution has positive skewness.

260 The mechanisms underlying log-normal like distributions of activity of individual neurons *in vivo* are not
261 well understood [5], and may involve both cell-intrinsic and network phenomena. Our model does not
262 clarify the potential contribution of the former, since all cell types were tuned to the same target rates
263 (apart from the excitatory/inhibitory distinction), but sheds light on the latter. We found that, when
264 similar levels of background excitation were applied to all cells, spontaneous rates were either zero or
265 uniformly close to the mean, whereas log-normally distributed strength of background inputs (see **Fig.
266 S1c**) resulted in spontaneous firing rates distributed over 2 or more decades. In a highly simplified
267 approximation, one may consider that under visual stimulation cells preferring a given stimulus may
268 increase their firing by about an order of magnitude, whereas activity of all other cells remains more or
269 less the same as under no stimulation. Thus, given log-normal distribution of spontaneous rates, one
270 expects that the distribution under visual stimulation remains largely the same, perhaps slightly wider,
271 which is indeed what we observe (**Fig. 3a**). This emphasizes the importance of enabling log-normal like
272 distribution of spontaneous rates, and our work suggests that log-normally distributed strength of
273 inputs that cells receive (potentially, from non-local sources) may play a big role in this, although other
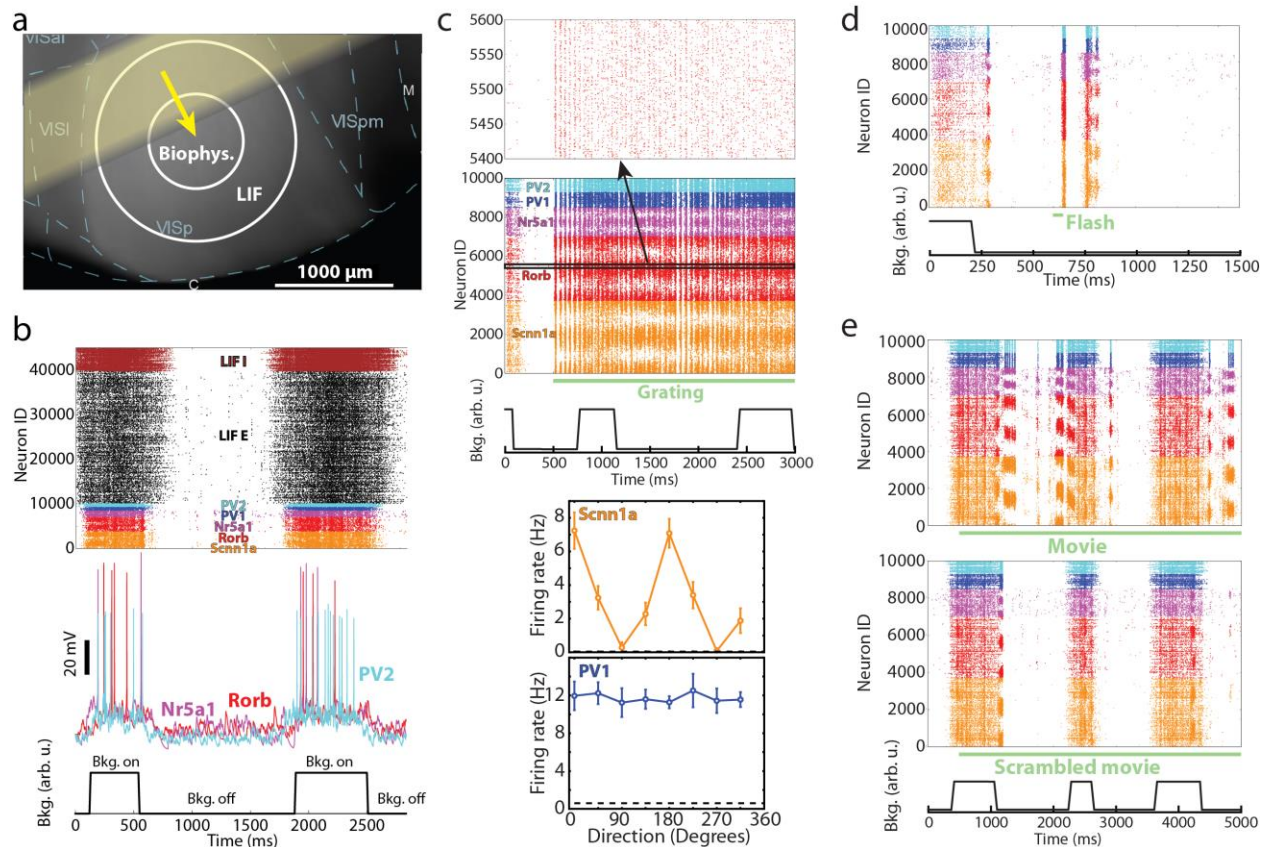274 mechanisms cannot be excluded.

Figure 2. Examples of simulated responses to various visual stimuli. (a) Spontaneous activity in the model was generated by waves of background excitation ("Bkg. on", yellow arrow denotes the direction of motion of the yellow bar-like region) alternated with intervals of no background excitation ("Bkg. off"). (b) Model activity in a gray screen trial. Examples of membrane potential traces from simulated biophysical cells are in the middle. (c) Spike raster in response to a drifting grating (TF = 4 Hz, at 0 degrees direction). Bottom, example orientation tuning curves for an excitatory and inhibitory cell from simulation. (d) Spikes in response to a 50 ms full-field flash. (e) Spike raster for a single trial of a natural movie (top) and for a temporally scrambled version of the same movie (bottom). The raster in (b) shows all neurons and those in (c-e) for clarity show the 10,000 cells in the biophysical core of the model (inset on top of (c) zooms in on 200 cells). All rasters are examples from one trial; all trials used unique combinations of "Bkg. on" and "Bkg. off" states (shown at the bottom of plots), which overlapped (or not) in different ways with the visual stimuli.

10

289   Another aspect of activity that we checked was whether the magnitude of responses was consistent
290   with the experiment; presumably, it is important for network computations that cells of certain types
291   fire at certain rates in response to particular stimuli. For this purpose, we considered the rates of
292   spontaneous activity and maximal rates (R_{max}) in response to drifting gratings (**Fig. 3b**; see Methods for
293   definitions). The spontaneous rates were 0.5-1.0 Hz for excitatory and 1.5-2.0 Hz for inhibitory cells,
294   broadly consistent with our experimental measurements and published data [N6], and R_{max} levels were
295   also similar to experimental ones.

296   Furthermore, the L4 responses to gratings are known to exhibit orientation and direction selectivity
297   (e.g., [6, 7]). We found that the orientation selectivity index (OSI; see Methods) for excitatory cells was
298   ~0.4-0.5 on average, in excellent agreement with the experiments (**Fig. 3b**). For inhibitory cells, OSI was
299   ~0.05 on average, whereas the experimental value was ~0.3. The relatively low OSI values were due to
300   non-selective thalamic inputs and recurrent connectivity for inhibitory cells (see Methods), which were
301   chosen that way at model construction to conform to an often-expressed view that excitatory cells are
302   tuned and inhibitory fast-spiking cells are not. However, recent experiments [33], as well as our own
303   data (Fig. **3b**), suggest moderate levels of tuning for these neurons, and therefore future models will
304   need to reflect these observations better. Nevertheless, qualitatively the model already captures the
305   trend of better tuning of excitatory cells compared to inhibitory fast-spiking cells. Another much studied
306   aspect of orientation tuning in the cortex is its contrast invariance in excitatory neurons (see, e.g., [8,
307   9]).   Excitatory neurons in our simulations were strongly orientation-tuned for contrast as low as 10%
308   (**Fig. S5c**). We computed the differences of the half-width at half-height of the tuning curves at high and
309   low contrasts for each cell (ΔHWHH) and found (**Fig. S5d**) that the distribution of ΔHWHH sharply
310   peaked near zero. On average, the difference was 4 +/- 5 degrees for 80% vs. 10% and –2 +/- 4 degrees
311   for 80% vs. 30% contrasts (i.e., the average was within the standard deviation in both cases). Thus, our
312   model exhibited substantial robustness of tuning curves to contrast (although perhaps not to the full
313   extent of the real mouse V1 [8]).

314   By contrast to OSI, the model performed poorly on the direction selectivity index (DSI; **Fig. 3b**), which
315   was close to zero in simulations, whereas experimentally it was ~0.4-0.5. This was due to the extreme
316   simplicity of the LGN inputs, which were constructed based on the experimental data, but at this point
317   did not include all types of LGN activity observed experimentally [7, 17, 21]. In particular, for simplicity,
318   we did not include the sustained LGN responses (i.e., all LGN filters produced transient responses),
319   whereas the most recent experimental data suggest a critical role for the interplay between sustained
320   and transient LGN inputs in generating direction selectivity in V1 [23]. Proper incorporation of direction
321   selectivity is the subject of ongoing work on the next generation of the model.

322   Another important aspect of neuronal activity *in vivo* is the population-level oscillatory rhythms, which
323   are observed in a variety of frequency bands. Whereas oscillations at many of such frequencies are
324   likely caused by non-local interactions in the brain, and therefore cannot be expected to arise in an
325   isolated L4 model, some of them may be generated locally. Indeed, our simulations exhibited
326   oscillations in the 15-50 Hz range (sometimes referred to as "mouse gamma"), with a peak at ~20 Hz
327   (**Fig. 3c**). This is consistent with extracellular electrophysiology data [10], which exhibits a particularly
328   strong peak at similar frequencies in L4.

329   Global luminance changes present another challenge to models, due to simultaneous engagement of all
330   cells by these stimuli. We studied responses to 50 ms full-field flashes and observed, in both experiment

331   and simulations, that a sharp and fast peak in activity was evoked by the first white-to-gray transition,
332   followed by a second smaller and wider peak (**Figs. 2d, 3d**). The magnitude of the first peak was about
333   2-4 times higher in simulation than in the experiment, whereas that of the second peak was
334   approximately the same, and the time course of the response was uniformly ~2-fold faster in
335   simulations (**Fig. 3d, e** and **Fig. S5b**). These differences were most likely again caused by the absence of
336   sustained LGN responses in the model. Importantly, however, in both simulations and experiments, the
337   second peak was delayed – instead of 50 ms (the flash duration), it appeared 100 ms after the first (200
338   ms in the experiment). This reflects a known phenomenon of suppression following luminance change,
339   where the second peak corresponds to release from inhibition (e.g., [48, 49]). Thus, qualitatively the
340   model reproduces well the critical features of cortical responses to global luminance change, which
341   likely affect perception of visual stimuli (such as in, e.g., luminance-induced visual masking).

342   Finally, an essential observation is that natural scenes evoke responses in V1 that are substantially
343   different from those evoked by artificial stimuli such as gratings. This was the case in simulations – for
344   example, responses to a natural movie in **Fig. 2e** were very distinct from those to a horizontally drifting
345   grating in **Fig. 2c** (both use the same ID labels). For a grating, cells with certain IDs respond strongly
346   throughout the simulation (as they prefer the grating's orientation). By contrast, natural movies evoked
347   episodes of concerted responses in distinct populations of cells (which share similar orientation
348   preference). Notably, such concerted responses were mostly absent when movie frames were shuffled
349   in time (**Fig. 2e**, bottom).   To quantify the differences, we computed lifetime sparsity for each cell
350   following Vinje and Gallant [50] (see Methods). Sparsity was higher for movies than for gratings (**Fig. 3f**)
351   in both simulations and experiments, consistent with previous observations (including Ca^{2+} imaging
352   [16]): 0.77+/-0.16 in simulation vs. 0.71+/-0.22 in experiments for movies and 0.64+/-0.14 vs. 0.65+/-
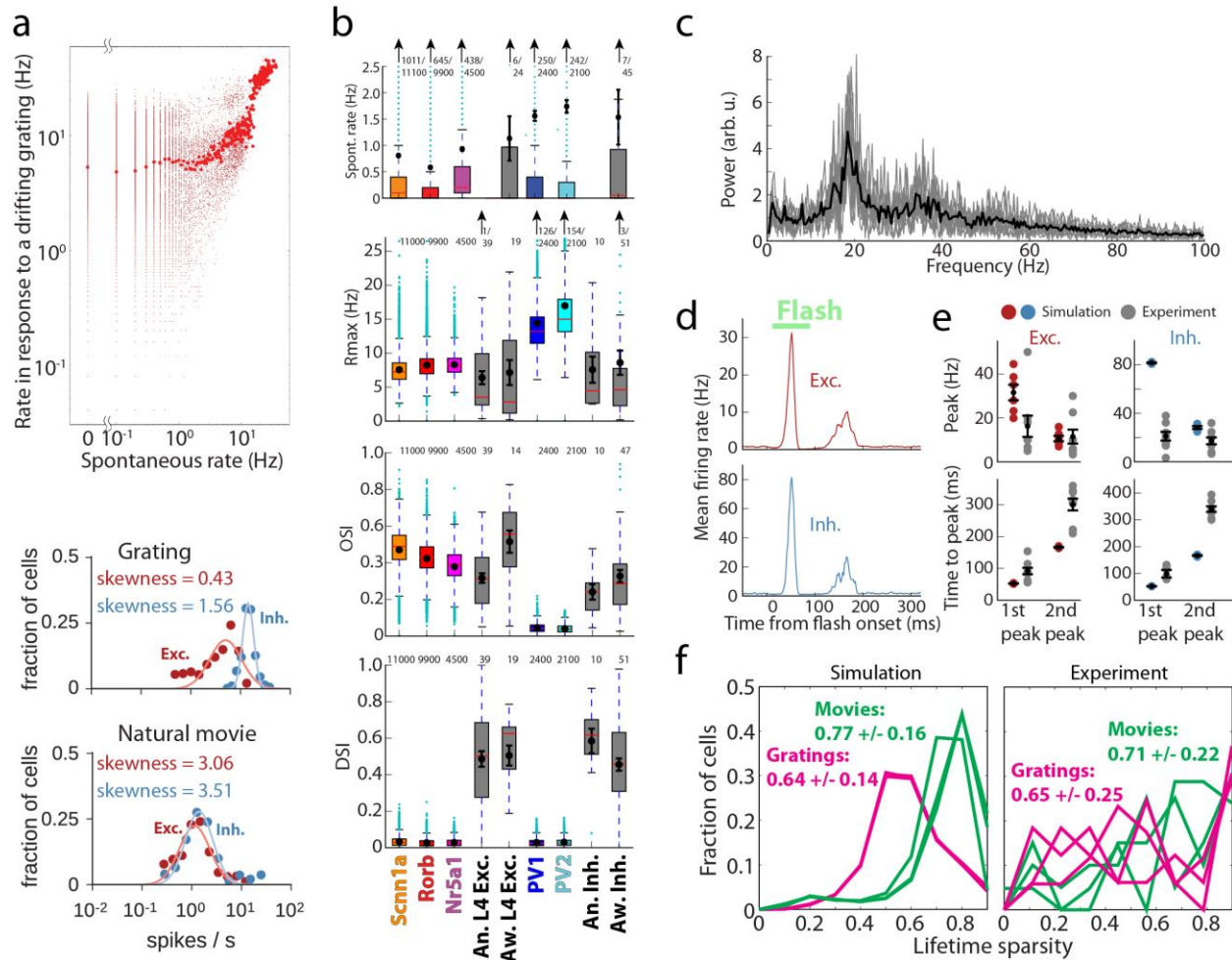353   0.25 for gratings.

354

355

12

356

Figure 3. Benchmarking the simulation results. (a) Log-normal like distribution of firing rates. Top, firing rates of all biophysical cells from three models during spontaneous activity and in response to a drifting grating, averaged over 10 trials. Large red dots are firing rates averaged over all cells in 0.1 Hz bins over the spontaneous activity axis. Bottom, examples of firing rate distributions on a log scale for a single trial. Solid lines indicate log-normal fits of the data. (b) Comparison of the spontaneous rates, maximal rates in response to gratings (R_{max}), orientation selectivity index (OSI), and direction selectivity index (DSI) between the simulation (by cell type, color) and experimental measurements using extracellular electrophysiology (gray). See Methods for details on the elements of the box plots shown here and in other figures. "An." – experiments in anesthetized mice, "Aw." – in awake mice. (c) The local field potential (LFP; see Methods) measured at the center of the L4 model, for a drifting grating. The spectra from 10 trials are shown in gray, and the averaged spectrum is in black. (d) The model PSTH in response to a 50 ms flash (average over all biophysical excitatory cells, all models, and all trials, in 2 ms bins). (e) The magnitude and time-to-peak (from flash onset) for the first and second peaks of the response to the 50 ms flash, for both simulation and electrophysiological data. (f) Distributions of lifetime sparsity of simulated and experimental responses of excitatory neurons, computed for three directions of a grating (0, 45, and 90 degrees) and for three movies. See Methods for details on computing all values presented.
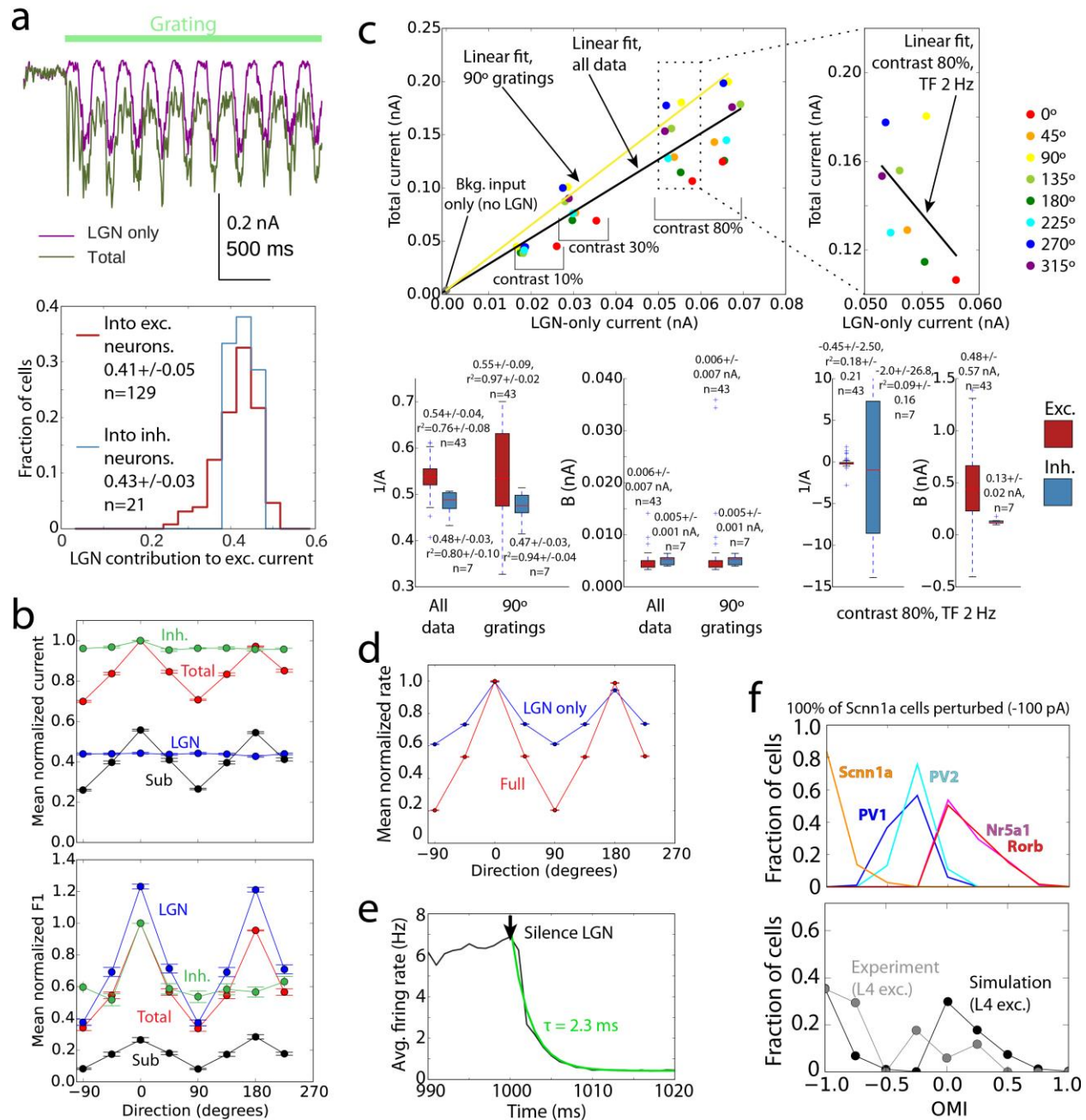
13

Figure 4. Mechanistic characterization of the model. (a) Cortical amplification of the LGN inputs. The excitatory currents (from the LGN only, as well as total) in biophysical cells were measured using voltage clamp recordings. Top – an example; bottom – distributions of LGN contribution to the total excitatory current across excitatory and inhibitory cells (computed for each cell as the average current over time and over all trials of the preferred orientation). (b) Tuning curves for the mean and F1 component of the total and LGN-only currents, and their difference ("Sub", i.e., the cortical component), as well as inhibitory current. The data for each cell were normalized to the peak value of the "Total" and shifted so that the preferred direction is at 0 degrees; averages and s.e.m. over all recorded excitatory cells are shown (TF = 2 Hz, contrast 80%). The inhibitory currents were normalized and aligned to their own peak values, since their magnitude is significantly higher than that of excitatory currents. (c) Amplification of

14

385   excitatory current. Top, the total current vs. the LGN-only current, for an individual Rorb cell (each point
386   is an average over time and over 10 trials). Linear fits ($I_{tot} = A\, I_{LGN} + B$) are shown for data
387   aggregated from all grating directions, TFs, and contrasts (black), for one selected direction (yellow), and
388   for a fixed contrast and TF (i.e., representing a sample direction tuning curve; right plot). Bottom,
389   summary of linear fits across all cells analyzed. (d) Tuning curves for mean firing rate in full network
390   simulations ("Full", red) and in simulations where all connections except the feedforward connections
391   from the LGN were removed ("LGN only", blue). The data for each cell were normalized to the peak
392   value of the "Full" and shifted so that the preferred direction is at 0 degrees; averages and s.e.m. over
393   all excitatory cells are shown (TF = 2 Hz, contrast 80%). (e) Simulations of responses to a drifting grating,
394   with the LGN activity switched off at 1000 ms. The black curve is the firing rate averaged over all cells,
395   models, and trials; green is the exponential fit. (f) Distribution of the optogenetic modulation index
396   (OMI) by cell type in responses to gratings, for simulations of optogenetic silencing of the Scnn1a
397   population (top). Combined distribution for all biophysical excitatory cells is compared to the
398   experimental result (bottom).

399

Mechanisms underlying neural activity and computation in the L4 circuit

400

401 We further used the model to shed light on the mechanisms that determine patterns of neural activity
402 and computations performed by the L4 circuit. One important question is to what extent the L4 activity
403 and computations are inherited from the input regions (here, LGN) vs. being shaped by intrinsic,
404 recurrent connectivity (see, e.g., [51]). To investigate this, in addition to regular ("Full") simulations, we
405 performed a number of simulations where recurrent and background connections were removed, so
406 that neurons received LGN inputs only ("LGN only"). Using *in silico* voltage clamp (see Methods), we
407 measured (**Fig. 4a**) synaptic excitatory currents at cells' somata – from the LGN only, I_{LGN}, and the total,
408 I_{tot} – and found that, for preferred directions of 2 Hz drifting gratings, the fraction of I_{tot} contributed by
409 I_{LGN} was 0.41+/-0.05 for excitatory cells, in good agreement with experiment (0.36+/-0.02 [17]). Also in
410 agreement with experiment [17], the mean I_{LGN} was untuned, since individual LGN filters were mostly
411 untuned [17] (but see [19, 20]), whereas mean I_{tot} and $I_{sub} = I_{tot} - I_{LGN}$ (i.e., the current due to
412 recurrent connections) were well tuned to the grating orientation (**Fig. 4b**), and F1 components (i.e., the
413 amplitude of the mode at the stimulus frequency; see Methods) of all of these currents were tuned.
414 Besides these features that were consistent with experimental recordings [17], one distinction was
415 observed: the F1 component of I_{sub} was substantially smaller than that of I_{LGN} or I_{tot} (**Fig. 4b**) and the
416 temporal dynamics of I_{sub} was in antiphase with that of I_{LGN} (**Fig. S6a**). This turned out to be a space
417 clamp artefact, where a stronger I_{LGN} current increases the membrane voltage at the synapses,
418 resulting in weaker driving force for recurrent excitation and, therefore, antiphase relationship of I_{LGN}
419 and I_{sub}; simulations where LGN current was removed from the recorded cells exhibited I_{sub} with no
420 oscillations at the grating frequency (**Fig. S6a**). Thus, the overall picture was that the I_{LGN} mean was
421 untuned whereas its F1 component was; the recurrent connections added current that was tuned
422 overall, but was not time-modulated (whereas in the experiment [17] it is time-modulated); and the
423 resulting total current was tuned in both mean and F1. The inhibitory currents were mostly untuned at
424 the level of both the mean and F1 (**Fig. 4b**); the F1 did show a preference to orientation, but its
425 magnitude was only a few percent of the mean and the current was not strongly modulated in time (**Fig.
426 S6a**).

427 Comparing mean I_{tot} and I_{LGN} of individual cells (**Fig. 4c**) for all grating conditions (i.e., not only the
428 preferred one shown in **Fig. 4a**) and different contrasts, we observed a complex dependence. The
429 relationship of I_{tot} with I_{LGN} was essentially linear along the contrast dimension (the quality of the
430 linear fit,

431

432 $$I_{tot} = A\,I_{LGN} + B,$$

433

434 was r²=76% for excitatory cells for all conditions, and 97% for a specific grating direction), consistent
435 with the prediction of an earlier, much simpler self-consistent model [51], but highly non-linear for the
436 orientation dimension (r²=18%). The latter was the consequence of the mean of I_{LGN} being untuned to
437 orientation, whereas the tuned current from recurrent connections made the mean of I_{tot} highly tuned
438 (**Fig. 4b**). Due to the same reason, the amplification factor A was approximately 2 across all conditions
439 (since B was very small on average, A can be thought of as the inverse of the LGN contribution

16

440 described above; across all conditions $1/A = 0.54$+/-0.04, **Fig. 4c**), whereas for the preferred orientation
441 it was 1/0.41=2.44 (as the LGN contribution at the preferred orientation was 0.41+/-0.05, **Fig. 4a**).

442 How do these relationships between currents shape the properties of the spiking output? We found
443 that the OSI in L4 at the level of spikes was inherited from the combined LGN inputs to each cell [17],
444 producing weakly selective output, and was strongly increased by recurrent connections (**Figs. 4d**, **S6b**).
445 Generally, the relationship between the rates in Full and LGN only simulations (**Fig. S6c**) was not close to
446 linear (attempting a linear fit

447

448 $$f_{Full} = A_f \, f_{LGN} + B_f,$$

449

450 where f_{Full} and f_{LGN} are the firing rates in Full and LGN only simulations, and the parameters A_f and
451 B_f are marked with the subscript "f" to distinguish them from the parameters of linear fit of currents
452 above, we found r^2=50% for all conditions and 65% for one grating direction for excitatory cells). The
453 firing rates at fixed contrast and TF exhibited a much more linear relationship (r^2=88%), but only locally –
454 the good linear fit required negative values of parameter B_f (-4+/-3 Hz on average), which is non-
455 physiological given that B_f is the firing rate of the cell under the conditions when the firing rate induced
456 by the LGN-only input is zero. Thus, overall the relationship was non-linear, but close to linear past the
457 firing threshold for LGN-only inputs. Interestingly, the overall effect of recurrent connections on the
458 spiking output in our model was that of suppression, as the Full-network firing rates at non-preferred
459 orientations tended to be smaller than LGN-only rates (**Fig. 4d** and **Fig. S6c**, top right), and only at the
460 preferred orientations Full-network firing reached the same rates as in the LGN-only case.
461 Consequently, R_{max} values were approximately the same in the Full and LGN-only cases (**Fig. S6b**).

462 To investigate the L4 circuit mechanisms further, we performed *in silico* optogenetic silencing of LGN
463 inputs and of a subset of the circuit (see Methods). Despite the significant recurrent amplification, L4
464 activity shut down rapidly when the LGN spiking was silenced (**Fig. 4e**), in agreement with an analogous
465 experiment [18]. Although the time course of activity decay was faster in the model (2.3 vs. 9+/-2 ms,
466 likely due to the absence of excitatory stimulation from other cortical regions), otherwise the effect of
467 LGN silencing was the same. The widespread and powerful intracortical inhibition appears to be the
468 most plausible driving force behind this effect. We then separately silenced the Scnn1a population of
469 excitatory cells in simulations and conducted analogous experiments *in vivo* (using Archaeorhodopsin-
470 mediated silencing on randomly selected trials during presentation of TF = 2 Hz drifting gratings, while
471 extracellular multielectrode recordings were performed, see Methods). Results were characterized by
472 converting firing rates with (f_p) and without ($f_{control}$) perturbation to the optogenetic modulation index
473 (OMI),

474 $$OMI = \frac{f_p - f_{control}}{f_p + f_{control}}$$

475 Simulations qualitatively agreed with experiment (**Figs. 4f, S7a, b**) in terms of the OMI distribution over
476 L4 excitatory cells (few inhibitory cells were recorded experimentally), which was approximately
477 bimodal, with one "lobe" concentrated close to -1 (totally silenced neurons) and the other near 0 (weak

478   or no effect). Due to challenges of recording form the thin layer 4, a small number of cells was obtained
479   in the experiment, but they all showed a consistent trend of OMI values belonging to one of these two
480   lobes (**Fig. S7a**). Whereas weak and/or sparse silencing of Scnn1a cells in simulations did not result in a
481   two-lobe distribution, a strong and dense silencing did (**Fig. S7c**), consistent with the experimental
482   perturbation that attempted to silence as many Scnn1a cells as possible. Simulations showed (**Fig. 4f**)
483   that the left lobe in the OMI distribution was due to near-complete silencing of Scnn1a cells. This
484   silencing reduced the amount of excitation in the network and resulted in moderate decrease of firing of
485   inhibitory cells. The net effect is that the firing rates of the other excitatory cell types (Rorb and Nr5a1)
486   remained almost unaffected – yielding the OMI lobe with values close to zero.

487
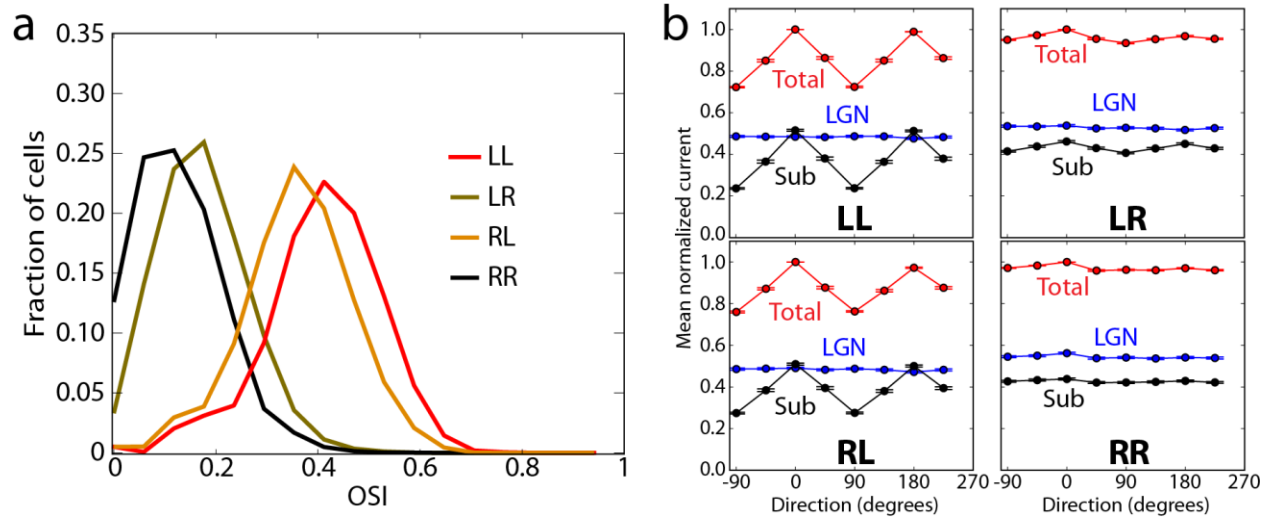
Figure 5. Like-to-like vs. random connectivity and synaptic weights. (a) Distribution of OSI for biophysical excitatory cells for the LL, RL, LR, and RR cases. (b) Tuning curves for the mean total and LGN-only currents, and their difference ("Sub", i.e., the cortical component). The data for each cell were normalized to the peak value of the "Total" and shifted so that the preferred direction is at 0 degrees; averages and s.e.m. over all recorded excitatory cells are shown (TF = 2 Hz, contrast 80%).

495   Finally, we investigated the effect of the logics of connections between L4 excitatory cells on the neural
496   activity and computation. In our regular models, a "like-to-like" ("L") rule [25, 26, 24, 29] was used for
497   both the connectivity and synaptic weights of excitatory-to-excitatory connections, based on the
498   anticipated orientation tuning of the cells (**Fig. 1c-e**); because the rule applied to both synaptic
499   connectivity and amplitude distributions, we refer to this set as "LL". We then studied three alternative
500   sets of models. In one, both the connectivity and weights were randomly ("R") assigned independently
501   of cell tuning ("RR"). The remaining two sets had the random rule applied to connectivity and like-to-
502   like to weights ("RL"), or vice versa ("LR"). Each set consisted of 3 models. Besides the "R" or "L" rules,
503   everything else was exactly the same between the four sets, including the probabilistic distance-
504   dependent connectivity (**Fig. 1c**).

505   Synaptic weights for all models were tuned following the same procedure (tuning only involved scaling
506   of weights uniformly across population, thus not affecting the "L" vs. "R" property, which applies to
507   individual cell pairs), resulting in similar levels of activity for training stimulus (grating) in all models. We
508   then assessed how functional properties differed. We found that OSIs were extremely reduced in the
509   RR set, with LR being only slightly better tuned, whereas RL came close to the original well-tuned LL set
510   (**Fig. 5a**). Because the mean LGN current was untuned in all models, the critical amplification of
511   orientation selectivity (**Fig. 4b-d**) came from the lateral L4 connections, which were well tuned in LL and
512   RL sets and poorly tuned in LR and RR sets (**Fig. 5b**). As a result, the total current as well as spiking
513   output was well tuned in LL and RL sets and barely tuned in LR and RR **(Fig. 5)**. This suggests a bigger
514   role of synaptic weights than connection probability in shaping network responses, which can be easily
515   understood since the "L" rule for weights results in low contributions from non-like-to-like connections,
516   even if such connections are present, thus effectively enforcing the "L" type connectivity.

517

518

519

520

521

522
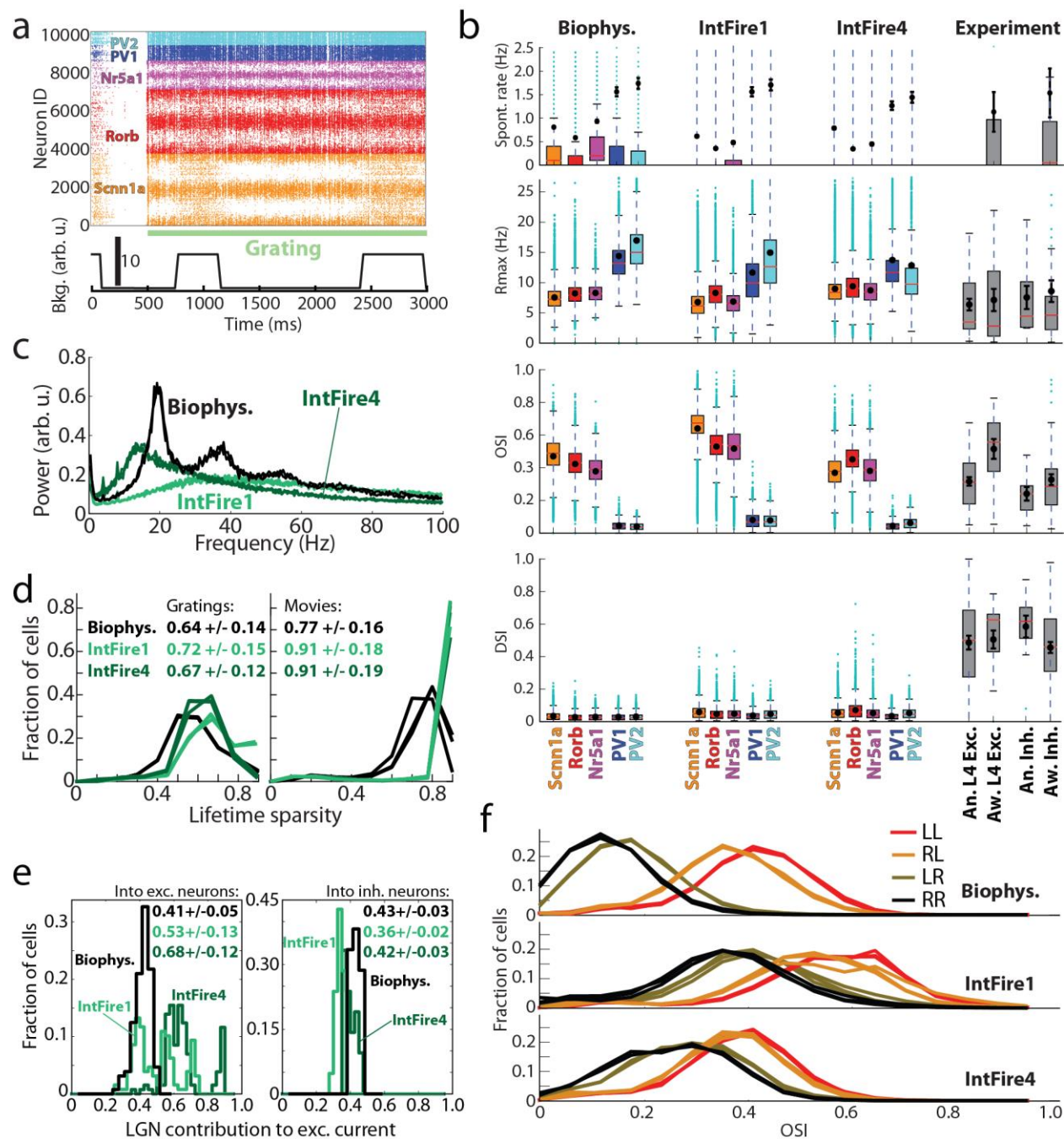
Figure 6. Comparison of biophysical and all-LIF simulations employing the IntFire1 or IntFire4 models. (a) An example spike raster in response to a drifting grating in an all-LIF IntFire1 simulation. (b) Spontaneous rate, R_{max}, OSI and DSI by cell type. (c) Spectra of multi-unit activity (weighted by $1/r$, where r is the distance from the cell to the center of the system; this is used as a proxy to LFP). (d) Distributions of lifetime sparsity of responses to gratings and movies, averaged over 10 trials. The data are for three directions of a grating (0, 45, and 90 degrees) and for three movies. (e) Distributions of

529   LGN contribution to the total excitatory synaptic inputs across excitatory and inhibitory cells (in the

530   IntFire1 and IntFire4 cases, this is computed for each cell as the average synaptic input over time and

531   over all trials of the preferred orientation; see Methods), for TF = 2 Hz drifting gratings. (f) Distribution

532   of OSI for excitatory cells for the LL, RL, LR, and RR cases.

533

Performance of a simplified model

How does the ability to reproduce experimental recordings depend on the level of granularity of the model? To address this question, we built two versions of a radically simplified model, where biophysical neurons and bi-exponential synapses were replaced by LIF neurons and either instantaneous "charge-dump" synapses (using NEURON's IntFire1 function) or synapses with exponential time dependence of synaptic current (NEURON's IntFire4 function). These all-LIF models used exactly the same cell-to-cell connections and inputs as the biophysical models and were optimized using the same protocol (see Methods).

The results of the all-LIF simulations were qualitatively similar to the results of biophysical simulations (**Fig. 6**), but specific quantitative distinctions were obvious. Although the overall appearance of responses (**Fig. 6a**) and mean values of spontaneous rates and R_{max} were similar to the biophysical case, the OSI values were elevated in the IntFire1 case (**Fig. 6b**). Most noticeable, the gamma oscillation was largely absent in the IntFire1 models (**Fig. 6c**). This was likely due to instantaneous synapses in IntFire1, since gamma oscillations [11, 12, 13, 14, 15] are thought to be strongly dependent on the properties of inhibitory perisomatic synapses [11, 14], and especially their time constants. Thus, removal of the appropriate synaptic kinetics from the large and distributed network model like ours may be expected to disrupt gamma oscillations. By contrast, the IntFire4 model employed a simple form of synaptic kinetics and produced oscillations in the range of 10-20 Hz, i.e., close to ~20 Hz gamma oscillation in the biophysical model (**Fig. 6c**).

Further distinctions were observed for sparsity values (**Fig. 6d**). The overall trend of higher sparsity for movies than for gratings was reproduced by both all-LIF models, but they both also exhibited higher sparsity values than the biophysical case and the experiment (**Fig. 3f**). Perhaps the most significant difference with the biophysical model was observed for the magnitude of cortical amplification (**Fig. 6e**) for excitatory cells (interestingly, inhibitory cells did not show substantial differences). The LGN contribution was 0.41+/-0.05 in the biophysical model and 0.36+/-0.02 in experiment [17], whereas it was 0.53+/-0.13 for IntFire1 and even higher, 0.68+/-0.12, for the otherwise more realistic IntFire4. The distributions of amplification values were also quite different in all-LIF models (**Fig. 6e**), exhibiting multiple peaks – apparently for the multiple excitatory cell types – instead of a single peak in the biophysical model. Finally, the functional connectivity had the same consequences in the all-LIF models as in the biophysical case – the orientation tuning was high for models with the LL or RL rules, and low for LR and RR (**Fig. 6f**). On the other hand, the small difference between the LL and RL cases, observed in the biophysical model, was mostly eliminated, and overall the OSIs were higher for the IntFire1 model and, in the RR and LR cases, for IntFire4 as well.

DISCUSSION

The promise of data-driven neuroscience modeling is in harnessing computing power to establish a platform for discovery that would work hand-in-hand with experiments. For that promise to materialize, models need to be biologically realistic in recapitulating knowledge about brain structure as well as in reproducing *in vivo* activity and computation. Doing either is difficult, and doing both together is more difficult yet, and has not been widely practiced (though, see, e.g., [2, 3, 4]). We described here a model of the L4 in mouse V1 that was built using a high degree of biological realism and simulated in a

23

575 framework of an *in silico* visual physiology experiment. We asked how well the model reproduces
576 activity observed *in vivo* across a variety of stimuli, which mechanisms underlie the activity and
577 computation in the modeled L4 circuit, and how the levels of simplification used in the model affect its
578 performance.

579 Despite the small training set of stimuli for which our model was optimized – a gray screen and a single
580 grating presentation for 0.5 s – it generalized well to a large test set of stimuli. The model reproduced
581 major features of *in vivo* observations with respect to, e.g., the magnitude of responses to gratings,
582 orientation selectivity, prominence of gamma oscillations, long-tailed distributions of firing rates,
583 lifetime sparsity for gratings and movies, magnitude of cortical amplification, and effect of optogenetic
584 perturbations of the LGN or the Scnn1a population in L4 (**Figs. 3, 4**). Such an agreement across stimulus
585 classes and types of observation is remarkable given that, although the model included a significant
586 degree of biological realism, many simplifications were used: neurons possessed active conductances
587 only at the soma, the variety of neuron models was limited to five unique single cell morphologies and
588 sets of membrane conductances, synapses had no short-term plasticity, LGN inputs were simplified,
589 connectivity was established via simple probabilistic rules, most known interneuron cell types [33] were
590 absent, and in fact the influence of most of V1 (L1, L2/3, L5, and L6) and the rest of the brain was
591 reduced to extremely simple background states. This may suggest that many of L4 computations are
592 produced by its local network, and other layers may play a primarily modulatory role – such as gain
593 control exerted by L6 [52] – as far as L4 activity is concerned.

594 Perhaps even more instructive than successes, some deficiencies were observed too. In terms of
595 reproducing *in vivo* activity, the most important issues were the absence of direction selectivity and too
596 fast responses to full-field flashes (**Fig. 3b,e**). Both appear to be due to the extreme simplicity of the
597 LGN inputs – in particular, the absence of sustained LGN responses in the model. This provides an
598 immediate direction for improving the model, especially based on the more recent experimental results
599 [23], which is the aim of ongoing work on the next model generation.
600
601 In applying the model to study mechanisms underlying the operation of the L4 circuit (**Figs.4, 5**), we
602 found the following principles. Tuning in L4 cells arose from combination of convergent LGN inputs, but
603 to reach physiological levels of selectivity, the functional like-to-like connectivity was essential (**Figs. 4d,
604 S6b, 5**). The effect was especially sensitive to synaptic weights, and less so to connectivity alone (**Fig. 5**),
605 because like-to-like weights effectively enforce like-to-like connectivity by scaling down contributions
606 from non-like-to-like connections. These results suggest that like-to-like rules, experimentally observed
607 in L2/3 [25, 26, 24, 29], are likely to be found in L4 as well, and may play an essential role in determining
608 functional information processing in the cortex.

609 The amplification of excitatory current in excitatory cells due to recurrent connections was by 2-3-fold
610 (**Fig. 4a, b, c**), in quantitative agreement with experimental measurements [17]. The amplification was
611 linear [51] along the contrast dimension (possibly, in part due to our LGN filters being linear), but highly
612 non-linear along the orientation dimension (**Fig. 4c**), since the total current was tuned to orientation,
613 whereas the LGN current was untuned [17] (**Fig. 4b**). Thus, overall the network amplification was
614 extensive and non-linear both at the level of currents and at the level of spiking output (**Fig. S6c**).
615 Despite such strong excitatory amplification, the whole circuit was controlled by even stronger
616 inhibition, which readily shut down the activity in the absence of the LGN input [18] (**Fig. 4e**).
617 Optogenetic suppression of a subpopulation of excitatory L4 neurons (Scnn1a) resulted in a clearly

24

618   bimodal distribution of firing rate changes both in simulation and in experiment (**Fig. 4f**), demonstrating
619   a compensatory effect in the circuit, where only the directly targeted Scnn1a cells were shut down,
620   whereas other cells approximately maintained their activity levels.

621   In terms of the mechanistic characterization of the circuit, another important insight again follows from
622   the model deficiency: we observed that the cortical component of the excitatory current ("Sub") into
623   excitatory neurons was tuned to orientation, but poorly modulated in time (**Figs. 4b, S6a**), whereas in
624   the experiment it was strongly modulated at the grating frequency and closely matched the phase of the
625   LGN input [17]. In the model, this "Sub" component is tuned because of the like-to-like connectivity
626   rule, where cells receiving similarly oriented LGN inputs have higher connection probability and stronger
627   synapses. However, this rule does not take phase into account, and therefore, for a given target cell, all
628   source cells have different phases, explaining why the "Sub" current was not modulated at the grating
629   frequency. The fact that in the experiment "Sub" current is modulated and is in phase with the LGN
630   current indicates that the like-to-like connectivity is more sophisticated and includes also the phase
631   information [17]. This is consistent with reports in the literature [25, 24] that similarity in orientation
632   preference is a good but not the best predictor of connectivity and with theoretical ideas (e.g., [28]) that
633   lateral connections in the cortex are optimized to enhance features, such as extended lines in V1.

634   A further simplification of our network model, replacing all biophysical neurons by LIF units, preserved
635   most general trends in features of neuronal activity, but the quantitative agreement with experiment
636   suffered. The levels of orientation selectivity and sparsity of responses were altered (**Fig. 6b, d, f**). The
637   oscillations at the level of population activity were eliminated when instantaneous synaptic kinetics was
638   used and partially rescued with non-instantaneous synapses (**Fig. 6c**). Although further exploration is
639   necessary to find out how one can match the oscillations spectrum of the biophysical model with a
640   simpler network model, this result supports the idea that synaptic kinetics is important for generating
641   oscillations in the relevant regime (e.g., [11, 14]). Perhaps the most substantial difference with the
642   biophysical model was that the cortical amplification was not captured well by all-LIF models (**Fig. 6e**),
643   hinting that mechanisms shaping activity and computation in the L4 circuit may not be well represented
644   by these simpler models. Clearly, many modifications of the simpler models are possible that may
645   improve performance, and our results do not rule out that point-neuron simulations can be adequate
646   for studying cortical activity and function – in fact, our results are promising since many of the trends of
647   activity were reproduced qualitatively. But, they do suggest that careful characterization of the level of
648   representation used for modeling may be important and that biological detail may matter for faithful
649   representation of a variety of observables.

650   Overall, results reported here are encouraging in that, despite significant simplifications, many aspects
651   of activity and computation in the L4 circuit were captured by a data-driven model constructed in a
652   bottom-up fashion. We suggest that systematic data-driven modeling oriented towards mimicking *in*
653   *vivo* physiology experiments will be an important approach to take advantage of the modern large-scale
654   data collection efforts. Our software code, the model, and simulation results are made publicly
655   available (see SI) to enable further efforts in modeling *in vivo* activity and function.

656

657   **DATA AVAILABILITY**

658   Data generated or analyzed during this study are included in this published article in its supplementary
659   files; as specified in the SI, larger volumes of the data are made available online, and additional raw data
660   is available on request (per cost for data medium and shipping). Modeling and analysis also involved
661   data that are already publicly available (Allen Brain Observatory [53] and Allen Cell Types Database [31]).

662

663   **CODE AVAILABILITY**

664   The software code used to build models, perform simulations, and perform analysis is included in this
665   published article in its supplementary files.

666

667   **AUTHOR CONTRIBUTIONS**

668   A.A. and C.K. designed the overall study. J.B., N.dC., S.dV., D.D., S.D., N.W.G., R.I., T.J., J.L., B.L., S.M.,
669   S.R.O., R.C.R., G.S.-L., S.A.S., M.S., Q.W., and J.W. contributed to the design of models and simulations,
670   supplied data, and provided crucial advice. A.A., Y.N.B., N.C., D.F., N.W.G., S.G., R.I., Z.W., and Z.X.
671   developed modeling software, built models, and carried out simulations. N.dC., D.D., S.D., L.L., and
672   S.R.O. performed experiments. A.A., Y.N.B., M.B., N.dC., D.D., S.D., N.W.G., S.G., R.I., G.K.O., S.R.O.,
673   Z.W., and Z.X. analyzed the data. A.A. and C.K. wrote the manuscript with comments from all authors.

674

675   **ACKNOWLEDGEMENTS**

676   We are grateful to Gabe J. Murphy for helpful discussions. We thank the Allen Institute founders, Paul
677   G. Allen and Jody Allen, for their vision, encouragement and support.

678

679   **References**

680   [1] California Institute of Technology. Caltech Library Archives [Internet]. Available from:
681   http://archives-dc.library.caltech.edu/islandora/object/ct1:483

682   [2] Markram, H. et al. Reconstruction and Simulation of Neocortical Microcircuitry. *Cell* **163**, 456-492
683   (2015).

684   [3] Traub, R.D. et al. Single-column thalamocortical network model exhibiting gamma oscillations, sleep
685   spindles, and epileptogenic bursts. *J. Neurophysiol.* **93**, 2194-2232 (2005).

686   [4] Zhu W, Shelley M, and Shapley R. A neuronal network model of primary visual cortex explains spatial
687   frequency selectivity. *J. Comput. Neurosci.* **26**, 271 – 287 (2009).

688   [5] Buzsaki, G., and Mizuseki, K. The log-dynamic brain: how skewed distributions affect network
689   operations. *Nat Rev Neurosci.* **15**, 264–278 (2014).

690   [6] Niell CM, Stryker MP. Highly selective receptive fields in mouse visual cortex. *J Neurosci* **28**, 7520–
691   7536 (2008).

26

692   [7] Durand, S. et al. A comparison of visual response properties in the lateral geniculate nucleus and
693   primary visual cortex of awake and anesthetized mice. *J Neurosci* **36**, 12144—12156 (2016).

694   [8] Li, Y. et al. Broadening of Inhibitory Tuning Underlies Contrast-Dependent Sharpening of Orientation
695   Selectivity in Mouse Visual Cortex. *J. Neurosci.* **32**, 16466-16477 (2012).

696   [9] Finn, I.M., Priebe, N.J., and Ferster, D. The emergence of contrast-invariant orientation tuning in
697   simple cells of cat visual cortex. *Neuron* **54**, 137 – 152 (2007).

698   [10] Welle CG and Contreras D. Sensory-driven and spontaneous gamma oscillations engage distinct
699   cortical circuitry. *J. Neurophysiol.* **115**, 1821-1835 (2016).

700   [11] Brunel, N., and Wang, X.-J. What Determines the Frequency of Fast Network Oscillations with
701   Irregular Neural Discharges? *J. Neurophysiol.* **90**, 415–430 (2003).

702   [12] Borgers, C., and Kopell, N. Synchronization in Networks of Excitatory and Inhibitory Neurons with
703   Sparse, Random Connectivity. *Neural Computation* **15**, 509–538 (2003).

704   [13] Tiesinga, P, and Sejnowski TJ. Cortical enlightenment: are attentional gamma oscillations driven by
705   ING or PING? *Neuron* **63**, 727-732 (2009).

706   [14] Buzsaki, G., and Wang, X.-J. Mechanisms of gamma oscillations. *Annu Rev Neurosci.* **35**, 203-225
707   (2012).

708   [15] Bos, H., Diesmann, M., and Helias, M. Identifying Anatomical Origins of Coexisting Oscillations in
709   the Cortical Microcircuit. *PLoS Comput Biol.* **12**, e1005132 (2016).

710   [16] Froudarakis, E. et al. Population code in mouse V1 facilitates readout of natural scenes through
711   increased sparseness. *Nat. Neurosci.* **17**, 851-857 (2014).

712   [17] Lien AD, Scanziani M. Tuned thalamic excitation is amplified by visual cortical circuits. *Nat Neurosci*
713   **16**, 1315–1323 (2013).

714   [18] Reinhold, K., Lien, A.D., and Scanziani, M. Distinct recurrent versus afferent dynamics in cortical
715   visual processing. *Nature Neurosci.* **18**, 1789–1797 (2015).

716   [19] Kondo, S, and Ohki, K. Laminar differences in the orientation selectivity of geniculate afferents in
717   mouse primary visual cortex. *Nat Neurosci.* **19**, 316-319 (2016).

718   [20] Sun, W., et al. Thalamus provides layer 4 of primary visual cortex with orientation- and direction-
719   tuned inputs. *Nature Neurosci.* **19**, 308–315, (2016).

720   [21] Li, Y. et al. Linear Transformation of Thalamocortical input by Intracortical Excitation. *Nat Neurosci.*
721   **16**, 1324–1330 (2013).

722   [22] Morgenstern, N.A., Bourg, J., and Petreanu, L. Multilaminar networks of cortical neurons integrate
723   common inputs from sensory thalamus. *Nature Neurosci.* **19**, 1034–1040 (2016).

724   [23] Lien, A.D., and Scanziani, M. Emergence of Direction Selectivity at the Convergence of Thalamo-
725   Cortical Synapses in Visual Cortex. *bioRxiv*, 244293. DOI 10.1101/244293.

726 [24] Ko, H. et al. Functional specificity of local synaptic connections in neocortical networks. *Nature*
727 **473**, 87-91 (2011).

728 [25] Cossell L. et al. Functional organization of excitatory synaptic strength in primary visual cortex.
729 *Nature* **518**: 399-403 (2015).

730 [26] Lee, W.C. et al. Anatomy and function of an excitatory network in the visual cortex. *Nature* **532**:
731 370-374 (2016).

732 [27] Yoshimura, Y., Dantzker, J.L.M., and Callaway, E.M. Excitatory cortical neurons form fine-scale
733 functional networks. *Nature* **433**, 868-873 (2005).

734 [28] Iyer, R. and Mihalas, S. Cortical circuits implement optimal context integration. *bioRxiv*, 158360.
735 DOI 10.1101/158360 (2017).

736 [29] Wertz, A., Trenholm, S., Yonehara, K., Hillier, D., Raics, Z., Leinweber, M., Szalay, G., Ghanem, A.,
737 Keller, G., Rózsa, B., Conzelmann, K.-K., and Roska, B. Single-cell–initiated monosynaptic tracing reveals
738 layer-specific cortical network modules. *Science* **349**, 70-74 (2015).

739 [30] Gouwens, N. W. et al. Systematic generation of biophysically detailed models for diverse cortical
740 neuron types. *Nature Communications* **9**, 710 (2018).

741 [31] Allen Institute for Brain Science. Allen Cell Types Database [Internet]. Available from:
742 http://celltypes.brain-map.org.

743 [32] Braitenberg, V. and Schuz, A. *Cortex: Statistics and Geometry of Neuronal Connectivity*. Berlin:
744 Springer (1998).

745 [33] Tremblay, R., Lee, S., and Rudy, B. GABAergic Interneurons in the Neocortex: From Cellular
746 Properties to Circuits, *Neuron* **91**, 260-292 (2016).

747 [34] Hines ML, Carnevale NT. The NEURON simulation environment. *Neural Comput.* **9**, 1179–1209
748 (1997).

749 [35] Gratiy, S. et al. BioNet: a Python interface to NEURON for modeling large-scale networks.
750 *Submitted.* Package available from: https://alleninstitute.github.io/bmtk/bionet.html.

751 [36] Perin R, Berger TK, Markram H. A synaptic organizing principle for cortical neuronal groups. *Proc*
752 *Natl Acad Sci USA* **108**, 5419–5424 (2011).

753 [37] Troyer, T.W., Krukowski, A., Priebe, N.J., Miller, K.D. Contrast-invariant orientation tuning in cat
754 visual cortex: Feedforward tuning and correlation-based intracortical connectivity. *J. Neurosci.* **18**, 5908–
755 5927 (1998).

756 [38] Krukowski, A.E. and Miller, K.D. Thalamocortical NMDA Conductances and Intracortical Inhibition
757 Can Explain Cortical Temporal Tuning. *Nature Neurosci.*, **4**, 424-430 (2001).

758 [39] Bopp, R., et al. An Ultrastructural Study of the Thalamic Input to Layer 4 of Primary Motor and
759 Primary Somatosensory Cortex in the Mouse. *J. Neurosci.* **37**, 2435-2448 (2017).

760   [40] Binzegger, T., Douglas R.J., and Martin K.A. A quantitative map of the circuit of cat primary visual
761   cortex. *J. Neurosci.* **29**, 8441-53 (2004).

762   [41] Sato, TK, Nauhaus, I, Carandini, M. Traveling waves in visual cortex. *Neuron* **75**, 218-229 (2012).

763   [42] Tan, AY, et al. Sensory stimulation shifts visual cortex from synchronous to asynchronous states.
764   *Nature* **509**, 226-229 (2014).

765   [43] McGinley, MJ, et al. Waking State: Rapid Variations Modulate Neural and Behavioral Responses.
766   *Neuron* **87**, 1143-1161 (2015).

767   [44] Harris, K.D., and Thiele, A. Cortical state and attention. *Nature Reviews Neurosci.* **12**, 509-523
768   (2011).

769   [45] Wu L-J, Li X, Chen T, Ren M, Zhuo M, Characterization of intracortical synaptic connections in the
770   mouse anterior cingulate cortex using dual patch clamp recording. *Mol Brain* **2**, 32 (2009).

771   [46] Prinz, A. A., Bucher, D., and Marder, E. Similar network activity from disparate circuit parameters.
772   *Nature Neurosci.* **7**, 1345-1352 (2004).

773   [47] Lefort, S., Tomm, C., Floyd Sarria, J.-C., and Petersen, C.C.H. The Excitatory Neuronal Network of
774   the C2 Barrel Column in Mouse Primary Somatosensory Cortex. *Neuron* **61**, 301–316 (2009).

775   [48] Tucker, T.R. and Fitzpatrick, D. Luminance-Evoked Inhibition in Primary Visual Cortex: A Transient
776   Veto of Simultaneous and Ongoing Response. *J. Neurosci.* **26**, 13537-13547 (2006).

777   [49] Macknik, S. L. and Martinez-Conde, S. The spatial and temporal effects of lateral inhibitory
778   networks and their relevance to the visibility of spatiotemporal edges. *Neurocomputing* **58-60**, 775–782
779   (2004).

780   [50] Vinje WE and Gallant JL. Natural stimulation of the nonclassical receptive field increases
781   information transmission efficiency in V1. *J. Neurosci.* **22**, 2904-2915 (2002).

782   [51] Douglas, R.J., et al. Recurrent excitation in neocortical circuits. *Science* **269**, 981-985 (1995).

783   [52] Olsen, S.R., Bortone, D.S., Adesnik, H., and Scanziani, M. Gain control by layer six in cortical circuits
784   of vision. Nature 483, 47–52 (2012).

785   [53] Allen Institute for Brain Science. Allen Brain Observatory – Visual Coding [Internet]. Available from:
786   http://observatory.brain-map.org/visualcoding/.

787

788

789

790   **METHODS**

791

792   *Model building and simulation details*

793   All simulations were performed with the parallelized code (available in *Supplementary Files*) written in
794   python 2.7 and employing NEURON 7.4 [34] as a simulation engine. Simulations were carried out
795   typically on 120 CPU cores (Intel Xeon CPU E5-2620 v2, 2.10GHz; 128 GB RAM per a 24-core node),
796   requiring ~1 hour to simulate 1 s.

797

798   *Network Composition*

799   The network model was constructed from five biophysically detailed models of individual neurons [30]
800   from an early version of the Allen Cell Types Database [31], and two models of leaky-integrate-and-fire
801   (LIF) neurons (one for excitatory type and one for inhibitory type). The biophysical models employed
802   passive conductances in the dendrites and 10 active conductances in the soma, including Na^+, K^+, and
803   Ca^{2+} conductances, as described in detail in [30]. The five models represented three types of excitatory
804   L4 neurons (expressing the genes Scnn1a, Rorb, and Nr5a1) and two types of fast-spiking parvalbumin-
805   expressing (PV) interneurons. Cells expressing these markers comprise the majority of neurons in L4 of
806   V1. These models consisted of 264 (Scnn1a), 141 (Rorb), 101 (Nr5a1), 121 (PV1), and 91 (PV2)
807   compartments. The LIF neuron models were implemented using the IntFire1() function of NEURON,
808   which contains two parameters – the time constant and the refractory period. The former was set to
809   the average time constant from the corresponding biophysical models (from Scnn1a, Rorb, and Nr5a1
810   for the excitatory LIF neuron and PV1 and PV2 for the inhibitory LIF neuron); the latter was 3 ms for both
811   LIF models. All the models are available in the *Supplementary Files* (see SI).

812   The 45,000 cells in the network model were distributed as follows: 3700 for Scnn1a, 3300 for Rorb, 1500
813   for Nr5a1, 800 for PV1, 700 for PV2, 29750 for excitatory LIF, and 5250 for inhibitory LIF. The cells were
814   distributed in a cylinder 100 μm in height; the biophysical cells occupied the inner core with the 400 μm
815   radius, and the LIF cells, the outer shell with the radii from 400 μm to 845 μm.

816   Three independent models were generated using different random seeds. These three models were
817   used for each connectivity case (LL, LR, RL, and RR, see Main Text). For each model, the recurrent
818   connectivity and synaptic weights (see below) differed across the LL, LR, RL, and RR cases, since different
819   connectivity/weight rules were applied; everything else was identical across these four cases.

820

821   *Connectivity within the Network*

822   For the purposes of establishing recurrent connections, all neurons were considered to belong to two
823   groups – excitatory (E; Scnn1a, Rorb, Nr5a1, and excitatory LIF) and inhibitory (I; PV1, PV2, and
824   inhibitory LIF). Four types of connections were established: E-to-E, E-to-I, I-to-E, and I-to-I. The
825   probability of connection was chosen as a product of a function dependent on the distance between the
826   somata of the two cells and the function dependent on the difference of the assigned preferred
827   orientation angle (see **Fig. 1**). The latter function was constant, 1.0, for E-to-I, I-to-E, and I-to-I, whereas

828 for E-to-E it differed depending on the model we assumed. The models with like-to-like connection
829 probability (LL and LR, see Main text) employed a linear function, starting at 1 for the zero difference in
830 the preferred orientation angle, and equal to 0.5 at 90 degrees difference; for the models with random
831 connection probability (RL and RR), the function was set to one. The distance dependent function was
832 linear, with the peak at zero distance (0.34 for E-to-E and 0.26 for E-to-I in the case of LL and LR models;
833 0.255 for both E-to-E and E-to-I in the case of RL and RR models; and 1.0 for I-to-E and I-to-I in all cases).
834 The linear decay was determined by the distance at which the function became zero (300 μm for E-to-E
835 and E-to-I, and 160 μm for I-to-E and I-to-I). For established connections, the number of synapses was
836 selected randomly with uniform probability between 3 and 7.

837 The numbers of synapses from different sources per neuron are not well established for the mouse
838 visual cortex, but are known approximately for cat [40], where, for the L4 excitatory cells (spiny stellate
839 cells projecting to L2/3 or L4, and for pyramidal cells), the number of incoming synapses is ~5,000-7,000.
840 Out of those, e.g., for pyramidal cells, ~1,100 synapses come from L4 excitatory cells, ~2,550 from
841 excitatory cells in other layers, and ~2,000 are excitatory with unassigned source. Assuming the same
842 distribution of sources for unassigned synapses, one can expect that ~1,700 excitatory synapses are
843 from L4 sources. Note that the number of synapses from LGN is ~100-150 in the cat cortex. Converting
844 these numbers to fractions, one finds that ~25-30% of all synapses are from the L4 excitatory sources,
845 55-60% from other excitatory sources, and 15-20% from inhibitory sources. For the inhibitory cells in L4,
846 the fractions are similar, but the total number of synapses is smaller (~3,250 synapses for basket cells).

847 We assumed similar fractions for the mouse visual cortex, except the number of synapses from the LGN,
848 for which we experimentally found a much larger number, ~1,000 per cell (see Main Text). Assuming
849 somewhat smaller number of synapses for mouse cells than for cat cells, we posited (**Table 1**) for the
850 purposes of our model that pyramidal cells in L4 of V1 receive ~6,000 synapses total, with ~1,000 (17%)
851 coming from LGN, ~2,000 (~33%) from L4 excitatory sources, and ~400 (~7%) from L4 PV$^+$ inhibitory
852 sources. The rest was not modeled explicitly (except for the background, see Main Text and below), as it
853 comes from other L4 inhibitory sources (PV$^-$ interneurons – presumably, another 7%, i.e., ~400 synapses)
854 and from excitatory sources from other layers and brain regions (~2,200, i.e., 36%), both of which were
855 not represented in the model. For the synapses from the LGN, we did not model explicitly all the LGN
856 cell types (see below), and thus restricted the number of LGN synapses to ~600 out of the expected
857 1,000 total. For simplicity, we assumed numbers for synapses from LGN and L4 neurons to the PV+ cells
858 to be similar in our model to the numbers used for pyramidal cells. Due to the randomness of
859 connections and of the number of synapses per connection, the actual number of synapses from L4
860 sources for each cell varied within ~10% from the average (**Fig. S1a**).

861

862 **Table 1.** Assumed average numbers of synapses per an excitatory cell in L4 of mouse V1. See text for
863 details.

From LGN	From L4 excitatory cells	From L4 PV$^+$ interneurons	From L4 PV$^-$ interneurons	From neurons in other layers and brain regions	**Total**
1,000	2,000	400	400	2,200	**6,000**

864

865 Thus, each cell in our simulations received on average ~3,000 synapses from other excitatory and
866 inhibitory cells in the L4 model and LGN sources. After building our models, including connectivity, we
867 found that, for recurrent connections among the L4 cells, excitatory neurons received connections from
868 490 +/- 20 and sent connections to 480 +/- 20 neurons on average, whereas inhibitory neurons received
869 connections from 490 +/- 20 and sent connections to 530 +/- 20 neurons on average. In addition, each
870 cell also received a small number of "background" synapses, as described below.

871 Synapses were distributed on the dendritic trees of the target cells randomly within certain distance
872 constraints, on the soma, basal, or apical processes, according to the literature (e.g., [32, 33, 40, 54, 55,
873 56, 57, 58]). Namely, all synapses to PV1 and PV2 cells were distributed on the soma and basal
874 dendrites without limitations. For Scnn1a, Rorb, and Nr5a1 cells, excitatory synapses from L4 and
875 background were placed on basal and apical dendrites, 30 to 150 μm from the soma, excitatory
876 synapses from LGN were placed on basal and apical dendrites, 0 to 150 μm from the soma, and
877 inhibitory synapses were placed on the soma and basal and apical dendrites, 0 to 50 μm from the soma.

878

879 *Model of background inputs*

880 Whereas the recurrent connections within L4 and the LGN inputs (see below) were modeled explicitly,
881 the connections from the rest of the brain were represented using a simple model of "background"
882 traveling waves (see Main Text). For producing the waves, we distributed 3,000 Poisson spike
883 generators in the x-y space covered by the model (the L4 plane), and drew random connections from
884 these generators to the modeled L4 cells if the distance between a generator and a cell's soma was
885 within 150 μm, allowing between 18 and 24 such connections per cell. This approximation of a small
886 number of connections (much fewer than what is expected for incoming connections per L4 pyramidal
887 cell from outside L4 or LGN) was chosen for simplicity and for reducing computing expense; in the
888 absence of heterogeneity in the population of sources, providing a much larger number of connections
889 does not appear necessary.

890 The background sources produced Poisson spike trains from a time dependent firing rate, *f(x, y, t),* which
891 was controlled by the plane traveling waves (see **Fig. 2**). The waves were pre-generated from a different
892 random seed for each simulation trial. The direction of each wave's movement in the x-y plane was
893 randomly selected, its width in the direction of movement was kept constant in time, in the
894 perpendicular direction the wave was infinite, and its magnitude was also constant and randomly
895 selected to be between 5 and 15 Hz. In the absence of the wave, *f(x, y, t)* for each spike generator was
896 set to zero, and it sharply rose to the value given by the wave's height when the wave moved through
897 the (x, y) location of the generator. The waves were produced so that they rarely overlapped, and thus
898 the firing rate of the spike generators mostly exhibited periods of silence and periods of constant firing
899 output, as waves swept through each generator's location (see **Fig. 2**).

900 The utilization of background traveling waves furnished a simple and computationally efficient analogue
901 of different cortical states. To approximate physiological observations with the choice of the wave
902 parameters, we performed a small set of patch-clamp recordings in the pyramidal cells (n=3, targeting
903 L2/3 neurons in V1 for easiness of access) of anesthetized mice. In the neural responses during

904   spontaneous activity (gray screen; **Fig. S1b**), we observed clearly distinct intervals of rest and baseline
905   depolarization, and found that on average the duration of depolarized states was 700+/-300 ms and the
906   interval between the end of one such state and beginning of the next was 1,100+/-600 ms, overall
907   consistent with observations illustrated in the literature (e.g., [43, 42]). Clearly, this is only one
908   measurement under particular conditions, and, generally speaking, the actual characteristics of the
909   cortical states, such as duration of the hyperpolarized state, interval between such states, and also
910   potentially gradations in the degree of depolarization or hyperpolarization, would depend on the type of
911   modulation one considers. These characteristics may exhibit a variety of time scales. Nevertheless, it
912   appears that largely these cortical states may be modulated on the time scale of 1,000 ms or longer, by
913   the order of magnitude. Therefore, for simplicity, for the L4 model we generated background waves
914   that lasted from 200 ms to 1,200 ms (i.e., 700 ms on average) and were separated by intervals of 250 ms
915   to 1,750 ms (i.e., 1,000 ms on average) – both parameters being drawn randomly for each wave from
916   uniform distributions. The spatial extent of each wave was set to 2,000 μm, and the propagation speed
917   was set based on that and on the randomly selected duration of the wave.

918   The remaining parameters were the number of synapses per connection from a spike generator to a L4
919   cell and the conductance amplitude of these synapses at the synapse site. The amplitudes were set to a
920   single number for cells of one type; the variation in the resulting postsynaptic potentials/currents
921   (PSPs/PSCs) was due to varying synapse number per connection and random placement of synapses on
922   the dendritic tree (see below for a general description of the choice of synaptic weights). First, the
923   weights for the background synapses were set so that the V_m of target cells was elevated by 10-15 mV
924   from rest during the wave condition (which was the amount of elevation we observed between the
925   depolarized and rest states in the patch clamp experiments), in purely feedforward regime in absence of
926   any other connections. The weights were then further adjusted to reproduce the spontaneous firing
927   rates in the context of the full network (see below).

928   The number of synapses per background connection was the remaining parameter that we used to
929   generate a long-tailed distribution of background input strengths, which we found to be important for
930   producing a skewed (log-normal-like) distribution of firing rates (see **Fig. 3a**), as observed experimentally
931   [5]. Specifically, for each L4 cell, the numbers of synapses for every background connection to that cell
932   were the same, but differed between cells. These numbers were drawn from a long-tailed distribution
933   heavily weighted towards 1 synapse, but permitting up to 16 synapses (**Fig. S1c**). As a result, most L4
934   cells received similar amount of background excitation, but small fractions of cells received much higher
935   amounts of background excitation.

936

937   *Synaptic characteristics*

938   Bi-exponential synapses (NEURON's Exp2Syn) were used for biophysical and instantaneous synapses for
939   LIF target cells; the reversal potential was -70 mV for inhibition and 0 mV for excitation. For simplicity,
940   synapses did not employ short-term or other plasticity rules and had 100% release probability. Although
941   presence of such properties is well documented for individual cortical synapses, especially *in vitro*, their
942   role in functional properties *in vivo* is not well understood. Short-term plasticity may be less prominent
943   *in vivo* than *in vitro* (due to saturation to baseline levels) [8], whereas non-deterministic nature of
944   individual synapses is somewhat alleviated by the fact that multiple such synapses are typically present

945   for each connection. The role of these properties *in vivo* is an important subject for future investigation.
946   In the current study, neglecting these properties lead to significant conceptual simplifications as well as
947   savings in computing power, and the generally good agreement of the neural activity in the simulations
948   with the experiment (see Main Text) suggest that the role of these properties may be subtle and not
949   straightforward to analyze. As a side observation, one should note that, because the modeled synapses
950   were deterministic, the synaptic weights we used are probably underestimated in terms of the
951   conductance values at the synapse location. However, the postsynaptic effects at the soma – peak PSPs
952   and PSCs – were found to be consistent with the experiment (see below).

953   No complete resource exists yet with a characterization of synaptic weights and kinetics in L4 of mouse
954   V1, and the literature on the subject of synaptic weights in general is large and somewhat disparate in
955   the details of experimental methods used and features recorded and reported (such as post-synaptic
956   potentials, or PSPs, vs. post-synaptic currents, or PSCs, definitions of time constants for PSP or PSC
957   kinetics, etc.). Therefore, choices of synaptic weights in our models were guided only approximately by
958   the existing literature on the synaptic properties of the cortex in various species (e.g., [25, 45, 47, 59,
959   60]), and for various cortical areas and layers (e.g., somatosensory [47] and anterior cingulate [45]
960   cortices). Because of the lack of a consistent benchmark, we aimed at restricting the synaptic weights
961   and time constants within approximately an order of magnitude of the values reported across a variety
962   of experimental studies. The kinetic parameters were fixed in the models, whereas the weights were
963   allowed to be varied globally (such as, e.g., uniformly scaling weights of all excitatory synapses on
964   Scnn1a biophysical cells by a multiplicative constant, etc.) at the optimization stage. The optimization
965   stage aimed at reproducing firing rates to a grating, spontaneous activity, and avoid epileptic-like time-
966   locked activity of all cells (see Main text). Once the weights were scaled so that these aims were
967   approximately reached, they were kept constant throughout all simulations for a given model.

968   The synaptic weights were given constant values for each connection type (namely, four source types –
969   excitatory from L4, inhibitory from L4, excitatory from LGN, and excitatory from background – to the
970   seven target types – Scnn1a, Rorb, Nr5a1, PV1, PV2, and excitatory and inhibitory LIF), which for the
971   biophysical cells corresponded to a constant value of the peak conductance at the synapse site. For the
972   models where like-to-like synaptic weights were employed (LL and RL, see Main Text), the uniform
973   synaptic weights from above were further multiplied by a factor F_w that depended on the difference
974   between the assigned preferred orientation angle between the two cells:

975
$$F_w = \exp\left(-\frac{\Delta\theta^2}{\sigma_\theta^2}\right),$$

976   where $\Delta\theta$ is the angle difference (defined within 90°), and $\sigma_\theta = 50°$ was used in all cases.

977   Despite weights at the synapse location being constant for most connection types, the actual PSPs or
978   PSCs at the soma were widely distributed, because synapses were randomly distributed on the dendritic
979   trees. The peak somatic PSCs for E-to-E synapses (**Fig. S1d**), for example, were observed in the model to
980   be within 2 orders of magnitude, consistent with experimental findings [54]. Their distribution on the
981   log scale was wide – i.e., similar to a skewed, lognormal distribution (or representable as a sum of a few
982   lognormal distributions) described in the literature [5]. These distributions were very similar between
983   the LL, RL, LR, and RR models, half of which employed constant E-to-E synaptic weights and other half
984   used F_w-modulated weights.

985   After models were optimized and simulated, we extracted a subset of synaptic connections (n=100, each
986   containing 3 to 7 synapses, as explained above) from each model for each connection type (E-to-E, E-to-
987   I, I-to-E, I-to-I). We computed the PSCs and PSPs in voltage clamp and current clamp, respectively, and
988   analyzed their peaks and time course (**Fig. S2**). For the current clamp measurements, current was not
989   injected, thus allowing for characterization of synaptic properties near cell resting voltage. The voltage
990   clamp measurements employed holding voltages of -70 mV and 0 mV to characterize excitatory and
991   inhibitory synapses, respectively. For the time course characterization, we computed time to peak (time
992   between the presynaptic spike and the peak), rise time (time between 20% and 80% of the peak at the
993   rise stage), time of decay (the time constant from an exponential fit to the time course of decay, from
994   80% to 20% of the peak value), and the width (width at the half-peak level).

995   Results of this analysis indicate that the characteristics of all PSPs and PSCs are, on average, very similar
996   between all the models (**Fig. S2**). The latter observation for the peak values is interesting, as the models
997   were optimized separately based on overall characterization of network dynamics, and in principle one
998   could expect bigger differences in synaptic weights (and, thus, PSP/PSC peaks) for the LL, LR, RL, and RR
999   models. Furthermore, characteristics of PSPs and PSCs in the models are broadly consistent with the
1000   values reported in the literature, typically within a factor of 2 or less (e.g., [45, 47]; one should also note
1001   differences between the cortical regions and layers, different preparations and experimental conditions,
1002   as well as the naturally wide range of observed values). The trends observed in the literature were
1003   reproduced as well, such as faster dynamics of postsynaptic events in PV cells than in excitatory cells
1004   and a higher amplitude of inhibitory synaptic currents (e.g., [45]).

1005

1006   *LGN filters*

1007   To enable simulations with arbitrary movies as visual stimuli, we developed a filter layer, the output of
1008   which was used to drive the L4 model, representing inputs from the lateral geniculate nucleus (LGN).
1009   The filters accepted movies (x,y,t-arrays) as inputs and produced time series of a firing rate as output.
1010   The output firing rates were taken to represent the rates of LGN neurons, which project to L4.

1011   We used 3,000 filters each for three filter types – transient ON, OFF, and ON/OFF [6], i.e., representing
1012   9,000 LGN cells. The transient types correspond to cells that produce an increase in firing rate to
1013   transitions from dark to bright (ON), bright to dark (OFF), or both (ON/OFF), such that the firing rate
1014   returns relatively quickly back to baseline levels after the change in scene. For simplicity, the sustained
1015   LGN cell types [6], for which the firing rate may differ substantially from the baseline after the initial
1016   transient (depending on the resulting brightness level), were neglected. The major reason for neglecting
1017   these types and overall representing the LGN inputs with rather simple filters was that little is known
1018   about how different LGN cell types combine their projections onto L4 neurons, and how properties of
1019   these projections are correlated with functional properties of the target cells.

1020   Each LGN filter was represented by one (for ON and OFF filters) or two (for ON/OFF filters) receptive
1021   subfields, which were described by the following equations (see **Fig. 1**). The linear response, $L(t)$, of a
1022   receptive subfield was given by

1023
$$L(t) = \int_o^t d\tau \iint dx\, dy\, D_t(\tau)D_S(x,y)S(x,y,t-\tau),$$

35

1024   where x and y are the coordinates in the visual space (angles), t is the time, $S(x, y, t)$ is the input signal
1025   (a movie), $D_t(t)$ is the temporal kernel, and $D_S(x, y)$ is the spatial kernel. For all operations with filters,
1026   we used a linear angle approximation for x and y (that is, replacing the tangent of an angle by the angle
1027   value in radians, which is approximately correct for small angles). The double-gaussian spatial kernel
1028   (center-surround) was used,

1029
$$D_S(x, y) = A_c \, exp\left(-\frac{(x - x_0)^2 + (y - y_0)^2}{2\sigma_C{}^2}\right) - A_S \, exp\left(-\frac{(x - x_0)^2 + (y - y_0)^2}{2\sigma_S{}^2}\right),$$

1030   where we used $A_S = A_C/6$, $\sigma_S = 2\sigma_C$. The temporal kernel had the form

1031
$$D_t(t) = k \, t \, \frac{exp(-k \, t)}{1 - \frac{k^2 t^2}{6}}.$$

1032   The input signal was grayscale, represented on a 0 to 255 scale (from black to white), with a time step of
1033   1 ms and the pixel size of 1.25° in x and y (the frames were 192x96 pixels). It was fed directly into ON-
1034   type receptive subfields, or converted to $255 - S(x, y, t)$ and then fed into OFF-type receptive
1035   subfields. The linear response $L(t)$ was then combined with the baseline rate R_0 and passed through a
1036   rectifying nonlinearity, resulting in the firing rate:

1037
$$R(t) = max(R_0 + L(t), 0).$$

1038   For the ON/OFF filter, $R(t)$ from the ON and OFF receptive subfields were summed, and the mean of
1039   the corresponding R_0 values was subtracted, to produce the final $R(t)$ output.

1040   The resulting firing rate $R(t)$ was converted to spike trains using a Poisson random process,
1041   independently for each LGN filter (**Fig. 7a**). The firing rate exhibited a transient at the beginning of each
1042   visual stimulus, due to transition from no visual stimulation to a movie. To avoid this artefact, we
1043   always prepended 500 ms of full-field gray screen to a movie used as a visual stimulus, and replaced the
1044   resulting first 500 ms of $R(t)$ simply by R_0.

1045   The centers of the individual filters, (x_0, y_0), were distributed randomly in the visual space, limited to
1046   approximately 130° x 90°. The two receptive subfields of each ON/OFF LGN cell were displaced with
1047   respect to each other (in random direction in x, y for each ON/OF cell), so as to enable orientation
1048   selectivity. Aside from that, the filters were axially symmetric, resulting in no orientation or direction
1049   selectivity. The temporal and spatial frequency (TF and SF) selectivity was thus primarily determined by
1050   the constants σ_C, σ_S, and k in the spatial and temporal kernels.

1051   A new set of filters has been created for each of the three instantiations of the LL model type. These
1052   three instantiations of filter sets were then used for the three models within the LR, RL, and RR types.

1053   The values of parameters for the filters were chosen randomly with a uniform probability within certain
1054   range (**Table S1**). The ranges were selected to produce approximately the same preferred SF and TF
1055   (0.05 cycles per degree, or cpd, and 4 Hz, respectively) across filters, which is approximately in the
1056   middle of the typical preferred SF and TF range in real LGN cells [6]. Although real LGN cells exhibit a
1057   wide range of preferred SF and TF values, we used the above simplification in order to avoid
1058   complexities of how different information processing channels with different SF and TF tuning converge
1059   on the L4 cells, as these aspects of feedforward connectivity from LGN to V1 are largely unknown. The

1060 specific choice of parameters also allowed for relatively wide tuning over SF and TF for our LGN filters,
1061 even though the peak was almost always at SF=0.05 cpd and TF=4 Hz. This is generally consistent with
1062 experimental observations, where most LGN cells exhibit smooth progression of diminishing responses
1063 away from preferred SF and TF, rather than very sharply tuned responses [6].

1064 The above requirements were used to select values of σ_C and k. The baseline firing rate, R_0, was
1065 selected to conform approximately to the levels of spontaneous activity exhibited by LGN cells [6] (**Table**
1066 **S1**). The remaining free parameter, A_c, was selected so that the maximal observed F0 component (see
1067 below) of the responses to gratings was 11-12 Hz (**Table S1**), also approximating experimental findings
1068 [6]; +/-10% variation was allowed for this parameter.

1069 It should be noted that for this parameterization and for analysis described below we used the
1070 definitions of the F0 and F1 components of responses to drifting gratings following Ref. [6]. Specifically,
1071 we used the cycle-averaged firing histograms for each cell (using the cycle period of the drifting grating
1072 stimulus); F0 was the mean rate computed from the histogram and F1 was the absolute value of the
1073 Fourier component at the frequency of the drifting grating stimulus (i.e., for a sine function, $a +$
1074 $b \sin(\omega t)$, $F_0 = a$ and $F_1 = |b|$).

1075 Response properties of instantiated filters were analyzed and are presented in **Table S1**. Example
1076 responses of a transient ON and transient ON/OFF filters to gratings, in terms of tuning to orientation,
1077 SF, and TF, are also shown in **Fig. 7b** (responses of transient OFF cells are very similar to those of
1078 transient ON cells, except being inverted with respect to dark vs. bright). These analyses show that
1079 indeed the filters are not selective to the orientation and direction (except for F1 responses for transient
1080 ON/OFF cells), and are tuned almost exclusively to SF=0.05 cycles per degree (cpd) and TF=4 Hz.
1081 However, the SF and TF tuning of individual cells (**Fig. 7b**) is relatively broad, as intended.

1082

1083 *Supplying inputs from LGN filters to L4 neurons*

1084 Feedforward connections from groups of LGN filters to the L4 cells were created based on the shared
1085 retinotopy. Whereas the LGN filters were defined in the visual space, the L4 cells were not, and for
1086 connecting them we introduced retinotopy in the L4 model by mapping the x, y coordinates (i.e., the
1087 plane of the layer) in the space of L4 cells to the x, y positions in the visual space. The center of the L4
1088 model was assumed to correspond to the center of the visual space (i.e., center of the eye field). The
1089 positions were mapped using the conversion factor (from physical to visual space) of 120°/mm in x and
1090 50°/mm in y, following the experimental observation that representation of azimuth and elevation on
1091 the surface of mouse V1 differs in length scale approximately by a factor of 2 [61]. With this mapping,
1092 each L4 cell was assigned an x,y position in the visual space.

1093 To connect LGN cells to L4 cells, we created separate "lasso" subfields for each of three LGN types
1094 (transient ON, OFF, and ON/OFF), independently for each L4 cell (**Fig. 7c**; see also **Fig. 1** in Main Text).
1095 As above, a linear angle approximation was used here. The three subfields were positioned around the
1096 visual-space x, y location of the L4 cell. The lasso subfields for inhibitory L4 target cells were bigger,
1097 more symmetric, and more overlapping than those for excitatory target cells, since experimental studies
1098 show that receptive fields of fast-spiking interneurons tend to be larger than those of excitatory cells in
1099 L4 and L2/3, and orientation selectivity of fast-spiking interneurons is also significantly lower (see, e.g.,

1100   [62]). Specifically, for target L4 cells of PV1, PV2, and inhibitory LIF types, all lasso subfields were

1101   centered at the L4 cell's position and were circular, with the diameter randomly selected from the range

1102   [15°, 20°]. For the excitatory target cells, the ON/OFF lasso subfield was centered at the L4 cell's

1103   position and was circular, whereas centers of the ON and OFF subfields were equidistant from the

1104   center, separated by an offset distance chosen randomly from the range of [10°, 11°] (thus enabling

1105   orientation selectivity and preference for a particular SF). These subfields were ellipsoidal (of equal size

1106   for a given target cell), with the ellipse aspect ratio being selected randomly from a range of [2.8, 3.0].

1107   The ellipse minor radius was chosen randomly from the range [3°, 4°], and the major radius was

1108   computed by multiplying the minor radius by the aspect ratio. The minor axis was oriented along the

1109   line connecting the center of the two subfields. The ON/OFF subfield radius was equal to the minor

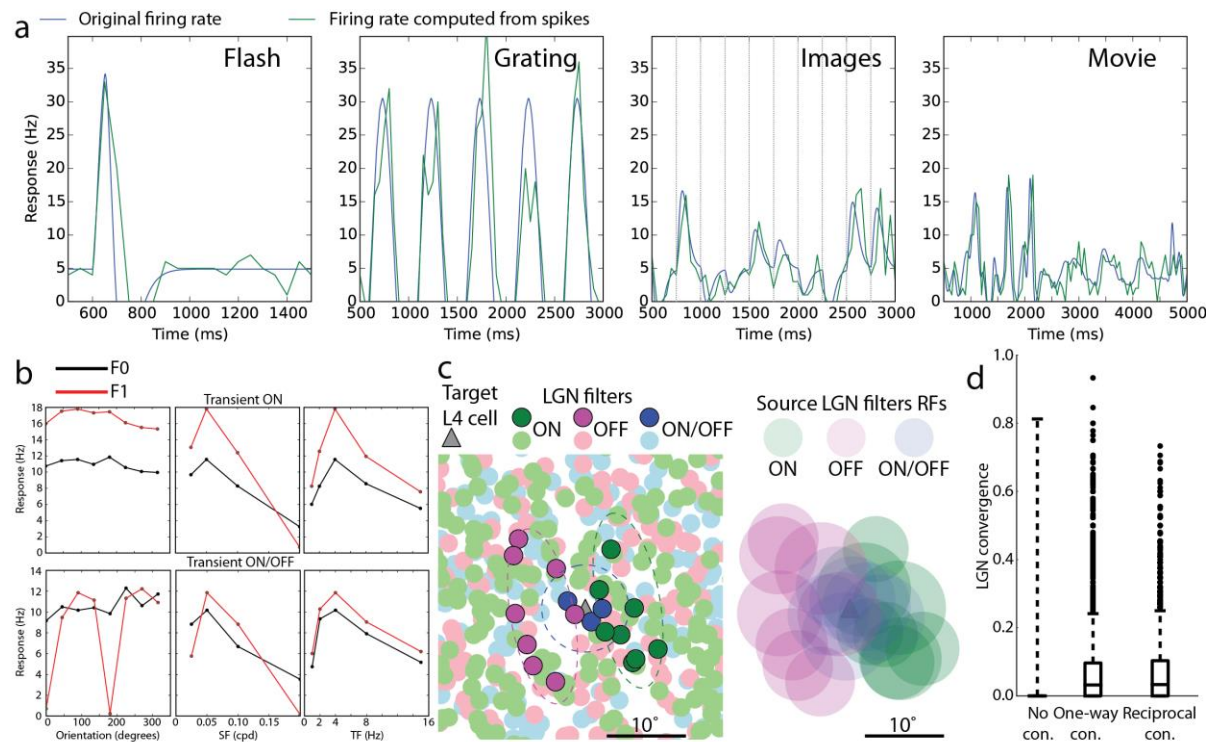1110   radius of these ellipses.

1111

1112

1113

Figure 7. LGN filters. (a) Example responses of a single filter to visual stimuli, as a time-dependent firing rate that is the filter output (blue) and the firing rate computed from generated spike trains, averaged over all trials (green). For clarity, the first 500 ms of each trace are not shown; during this interval, the rate is set to a constant corresponding to the level of spontaneous activity of the filter. The panel for images contains responses to 10 images shown in a sequence, 250 ms each. (b) F0 and F1 components of the responses to gratings for two example LGN filters. Tuning curves to orientation, SF, and TF are shown. The data points are averages from generated spike trains over time and over trials. (c) Connecting LGN filters to L4 cells. Geometry in the visual space is illustrated. The left panel shows centers of all filters present in a portion of the visual space around the mapped position of an example excitatory cell from L4. The dashed lines correspond to the "lasso" subfields around one illustrative L4 cell, used to capture input LGN filters of the ON, OFF, and ON/OFF type. The filters that are selected to send inputs to this L4 cells are in deep color; all other filters are dimmed. On the right, the same L4 cell with the filters selected to provide inputs to it are shown. For the filters, the approximate size of their receptive subfields is illustrated (a single subfield for ON or OFF filters and two subfields for ON/OFF filters; the radius of each RF circle is $2\sigma_C$). (d) Convergence of LGN connectivity onto L4 cells that are not connected to each other ("No con."), one-way connected ("One-way con."), and reciprocally connected ("Reciprocal con."). For each pair of L4 cells, the LGN convergence is defined as the number of LGN filters that connect to both cells divided by the sum of the numbers of LGN filters connected to each of the cells. The data are aggregated from three L4 models.

1133

1134   For the excitatory L4 target cells, the choice of the direction in which the ON and OFF lasso subfields
1135   were positioned (**Fig. 7c**) was determined by the assigned preferred orientation angle that was set for
1136   each L4 cell at model construction. The angle between the vector connecting the centers of the ON and
1137   OFF subfields and the (1, 0) vector in the visual space was chosen to coincide with this assigned
1138   preferred orientation angle. Note that the actual preferred orientation angle was determined by the
1139   network activity in the simulations, and generally speaking did differ (more or less) from the assigned
1140   one.

1141   Once all the lasso subfields were established for an L4 cell, the corresponding LGN cells were selected
1142   based on whether centers of their spatial kernels happened to be inside the subfields or not. Among
1143   those inside, a random set of LGN cells was selected, with the total number of each LGN type selected
1144   for one L4 target cell being capped at 15 for the inhibitory target cells and at 8 for the excitatory target
1145   cells (i.e., because we used 3 types of LGN cells, the maximum number of source LGN cells was 45 for
1146   inhibitory targets and 24 for excitatory targets). For the ON/OFF filters, the additional condition applied
1147   during the selection of sources, which required that selected filters were oriented (i.e., the axis
1148   connecting the centers of their ON and OFF subfield was oriented) within +/-15° from the assigned
1149   preferred orientation angle of the L4 cell. In terms of connections from individual LGN filters to L4 cells,
1150   after instantiating models we found broad diversity in the number of target L4 cells per LGN filter, from
1151   0 to several hundred; on average, one LGN filter connected to 100 +/- 170 L4 cells.

1152   Since the LGN filters used did not represent all the LGN cell types (specifically, no sustained types [6]),
1153   we assumed that the number of synapses they provided to the L4 cells was smaller than the total
1154   expected number of synapses from the LGN (~1,000, see Main Text). We thus set the number of
1155   synapses per each LGN filter connected to an L4 cell to be 30, resulting in approximately 600 synapses
1156   from the LGN for each L4 excitatory cell.

1157   The geometric constraints above (size and separation of the lasso fields, etc.) were chosen to reflect
1158   approximately the characteristics of the receptive fields of the LGN inputs to L4 excitatory cells, based
1159   on *in vivo* measurements of LGN-only currents into L4 cells, resulting from visual stimulation [7], and
1160   also taking into account typical sizes of the receptive fields of LGN cells themselves, based on
1161   extracellular electrophysiological measurements [6]. Arguably, the constraints we applied were
1162   representative of a typical case, but did not reflect the considerable diversity of the receptive field sizes
1163   and shapes [6, 7]. This was done for simplicity, as we aimed to represent well the responsiveness of the
1164   LGN and L4 cells to SFs and TFs that are in the middle of typical values that evoke robust responses *in
1165   vivo* (SF~0.05 cpd and TF~4Hz). Introducing more diversity would require further assumptions about
1166   connectivity from LGN to L4 and within L4, in absence of data. Another note is that the choice of the
1167   geometry of "lasso" subfields (high aspect ratios) may appear to contradict observations of the rather
1168   symmetrical and highly overlapping subfields for LGN inputs to L4 [7]. However, due to the large size of
1169   individual LGN filter receptive fields, the combined receptive subfields for the LGN inputs to L4 cells
1170   were not extremely elongated and exhibited certain degree of overlap (see example on the right in **Fig.
1171   7c**), similar to the experimental observations.

1172

1173   *Stimulation protocol*

1174   All simulations were performed with visual stimuli chosen among drifting gratings, natural movies,
1175   natural images, moving bars, and full-field flashes (**Fig. S3**, the first three are part of the stimulus set in
1176   the Allen Brain Observatory [53]). Separate simulations with uniformly gray screen were also carried out
1177   to characterize spontaneous activity. The list of all visual stimuli used for all model systems is presented
1178   in **Table S2**. All stimuli were mapped (linearly subsampled or interpolated) to 192x96 pixels and time
1179   step of 1 ms. Each trial was a separate simulation. Typically, 10 trials were simulated for each stimulus
1180   condition, with some exceptions specified below.

1181   Drifting gratings were square-wave alternating white and black stripes (typically at contrast 80%,
1182   although simulations with other contrasts were performed as well), drifting in the direction
1183   perpendicular to the stripes, at 0, 45, 90, 135, 180, 225, 270, or 315 degrees. For LGN filter
1184   characterization, 240 different gratings were used, in combinations of the 8 directions listed above, 6 SF
1185   (0.025, 0.05, 0.1, 0.2, 0.4, and 0.8 cpd), and 5 TF (1, 2, 4, 8, and 15 Hz). Due to the high computational
1186   expense associated with running simulations of the L4 model, and because the LGN filters were tuned to
1187   respond preferentially to SF ~ 0.05 cpd, for the full model simulations we used a subset of these 240
1188   conditions. A single SF=0.05 cpd and a few TF (typically, 2, 4, and 8 Hz) were used, with all 8 directions
1189   (**Table S2**). After the initial 500 ms of the gray screen, the gratings were presented for 2500 ms.

1190   The gratings were named from g1 to g240 in the following manner: starting from the minimal TF, SF, and
1191   direction angle for g1, the numbering increased first along the TF dimension, then along the SF
1192   dimension, and finally along the direction dimension. Thus, for example, g1, g2, g3, g4, and g5 were all
1193   at direction 0 degrees, SF=0.025 cpd, and TF varying from 1 to 15 Hz; or, gratings with a given SF and TF,
1194   such as SF = 0.05 cpd and TF = 4 Hz, had numbers that were always separated by 30 – g8, g38, g68, g98,
1195   g128, g158, g188, g218, for directions 0, 45, 90, 135, 180, 225, 270, and 315 degrees, respectively. (See
1196   *Supplementary Files* and **Table S2** for more details.)

1197   Natural movies were 3 clips from the opening scene of *Touch of Evil* [63, 53]. After the initial 500 ms of
1198   the gray screen, the movies were presented for 4500 ms. The three clips were named
1199   "TouchOfEvil_frames_N1_to_N2", where N1 and N2 were the first and last frame based on the
1200   sequence from the original movie clip (these frames were 33 ms each, as the movie was encoded at 30
1201   Hz rate; the clips used for simulations were upsampled to 1 kHz rate). The N1 and N2 were 1530 and
1202   1680 for the first clip, 3600 and 3750 for the second, and 5550 and 5700 for the third.

1203   For natural images, we used 10 examples taken from the Berkeley Segmentation Dataset [64] and the
1204   van Hateren Natural Image Dataset [65] (see also [53]). Each trial consisted of a 3000 ms long
1205   simulation, with the first 500 ms being the gray screen, and the rest covered by presentation of the 10
1206   images in a random sequence, for 250 ms each, without interruption. We carried out simulations of 100
1207   such trials, each named "imseq_i", where i was 0 to 99 ("imseq" standing for "image sequence").

1208   Moving bars were single white or black stripes on gray background, moving with constant velocity in a
1209   direction perpendicular to the stripe. Four conditions were assessed – a black or white vertical bar
1210   moving left to right, and a black or white horizontal bar moving bottom to top. The bars were
1211   approximately 4 degrees wide and moved with the velocity of 33.8 degrees per second. These
1212   simulations were named "Bbar_v50pixps_hor", "Bbar_v50pixps_vert", "Wbar_v50pixps_hor", and
1213   "Wbar_v50pixps_vert".

1214   Two types of full-field flashes were used (named "flash_1" and "flash_2"). For type 1, the screen was
1215   gray from 0 to 1000 ms, white from 1000 to 2000 ms, and gray again from 2000 to 3000 ms. For type 2,
1216   the screen was gray from 0 to 600 ms, white from 600 to 650 ms, and gray again from 650 to 1500 ms.

1217   Spontaneous activity was measured during 1000 ms long presentation of gray screen. Typically, 20 trials
1218   were used. These simulations were named "spont".

1219   All analysis generally disregarded the first 500 ms of each simulation, as an equilibration period (with
1220   gray screen presented as a visual stimulus during this time in all cases).

1221   For computational efficiency, a core set of stimuli from those described above was used for all systems
1222   (three cases each of LL, LR, RL, and RR), whereas the rest were applied in a targeted manner, primarily
1223   for the LL system (**Table S2**). Out of those, the richest set of stimuli was applied to model 2 of the LL
1224   type ("LL2").

1225   The LGN filter and background source projections to the L4 cells were generated independently for the 3
1226   models of the LL type and then reused for the 3 models each of the LR, RL, and RR types. The same
1227   procedure was applied to recurrent connections for LL and LR cases, as well as for RL and RR.
1228   Furthermore, each trial of visual stimulation was accompanied by an independently generated trial of
1229   the background activity. These were generated independently for the 3 models of the LL type, and then
1230   applied consistently to the 3 models of the LR, RL, and RR types. Thus, for example, the LGN and
1231   background feedforward connections, as well as LGN and background spike trains incoming to the L4
1232   cells on a particular trial of a given visual stimulus, were exactly the same between the models LL2, LR2,
1233   RL2, and RR2, but different from, e.g., LL1 or RL3.

1234

1235   *Modeling optogenetic perturbations*

1236   A number of simulations was performed to mimic the effects of optogenetic manipulations (see below
1237   for experimental details). The experimental optogenetic perturbation involved silencing of Scnn1a cells
1238   expressing ArchR through application of yellow light. To model such a perturbation, we injected
1239   hyperpolarizing current into somata of cells in our simulations (**Fig. S7**). We selected the cell type to be
1240   directly perturbed (typically Scnn1a), and a fraction of the cells in this cell type (all the cells in the cell
1241   type that were outside of this fraction did not receive current injections), and applied the current
1242   injections to those cells.

1243   Since the light spot used in the experiments was ~2 mm in diameter, in most simulations we applied
1244   perturbation over the whole area of our model (which was ~1.7 mm in diameter), including the LIF
1245   neurons. In a subset of simulations LIF neurons were not affected (this difference did not qualitatively
1246   affect the observed trends). Delivering direct current injections to LIF neurons was not supported in the
1247   NEURON implementation we used, and thus we opted for adding inhibitory synapses to LIF neurons that
1248   were selected for optogentic perturbations. A single such synapse was added to each silenced LIF
1249   neuron, and received a Poisson spike train at 100 Hz frequency. The synaptic weight was calibrated to
1250   result in the reduction of the LIF neuron's firing rate similar to that effected by a -100 pA current
1251   injection to the soma of biophysically detailed cells in a benchmark simulation. To represent different
1252   current injections, we linearly scaled the synaptic weights for these synapses on the LIF neurons. The LIF
1253   neurons were selected for receiving such perturbation based on the fraction of cells represented by the

42

1254 perturbed cell type and the fraction of cells selected for perturbation within the type. For example,
1255 Scnn1a constituted 43.5 % of all excitatory biophysical neurons; if we were applying optogenetic
1256 perturbation to 20% of Scnn1a biophysical cells, then we correspondingly applied perturbation via
1257 inhibitory synapses to 8.7 % of all LIF excitatory cells.

1258 The modeled optogenetic manipulation was applied at the beginning of the simulation and was
1259 maintained throughout the simulated time. For majority of these simulations, the injection current
1260 levels were -30, -50, -100, and -150 pA, whereas the fractions of Scnn1a population receiving such
1261 injections were 20, 50, and 100% (see **Table S2**).

1262 Optogenetic silencing of the LGN [8] (**Fig. 5d**) was modeled by eliminating all spikes coming from LGN
1263 filters starting at a desired time. For this study, such a time was always set to 1000 ms from the
1264 beginning of a simulation.

1265

1266 ***Experimental Methods***

1267 All experiments, animal treatment and surgical protocols were carried out with authorization from the
1268 Institutional Animal care and Use Committee of the Allen Institute in accordance with the Public Health
1269 Service (PHS) Policy on Humane Care and Use of Laboratory Animals.

1270
1271 *Experimental characterization of LGN-to-L4 synapses*
1272
1273 The synapse counts were performed using disectors on a systematic random sampling scheme. This
1274 allows for unbiased sampling and it has been used in other cortical areas and animals models (e.g. [66,
1275 39]). We cannot however identify the cell type of the post synaptic target and therefore we assume that
1276 thalamic neurons target cell types according to the available dendrite of each cell. Though exceptions to
1277 this rule have been found in other areas or animal models, the contribution of L5 and L6 apical dendrites
1278 to the overall dendritic length in L4 is expected to be smaller than the dendrite from L4 neurons and one
1279 expects that it will not change substantially the proportion of thalamic synapses onto L4 in ways that
1280 would affect the predictions of the model.

1281 We labeled thalamic boutons with immunohistochemistry for VGLUT2, selected sampling sites using
1282 rare systematic random sampling and then used the physical disector method introduced by [67] to
1283 perform the synaptic counts.

1284 *Histology*: Wild type mice were perfused with fixative (2% paraformaldehyde and 0.5% glutaraldehyde)
1285 and a series of 60 um coronal slices through primary visual cortex (V1) was taken, and alternating slices
1286 were processed for electron microscopy (EM) with immunohistochemistry, or processed with Nissl stain
1287 for light microscopy (LM).

1288 Slices selected for immunohistochemistry were incubated in anti vesicular glutamate transporter 2
1289 (VGLUT2) antibody. Nickel intensified diamino benzidin or silver intensified gold particles were used to
1290 visualize the labeled elements in the electron microscope (EM). Slices were then osmicated, dehydrated
1291 and embedded in Durcupan resin.

1292 We used as a primary antibody anti-VGLUT2 from Millipore, catalog number MAB5504 (lot 2322521).
1293 The secondary antibody was biotinylated-goat-anti-mouse IgG, from vector BA-9200 (lot X0623). Anti-
1294 VGLUT2 primary antibodies label thalamic terminals in several species including the mouse visual,
1295 somatosensory and motor cortices [68, 39] and it had been validated in layer 4 of mouse visual cortex by
1296 co-labeling of axons that have been injected in the thalamus [68]. The distribution of labeled terminals
1297 in this study matches the one previously observed in the cited works.

1298 *Sampling:* Slices, grids, sections and sampling sites were chosen using a systematic random sampling
1299 (SRS). A random number in the range of the number of slices was generated via computer, and used to
1300 select target coronal slices for the EM series. A general region of interest in V1 was then selected based
1301 on comparison to the cytoarchitecture of the immediately adjacent Nissl-stained sections. This region of
1302 interest, which contained layer 4, was excised from the EM slice, trimmed, and sectioned with an
1303 ultramicrotome at 40 nm thickness and serial section ribbons collected onto copper grids. Labeled
1304 terminals were then examined and photographed in a Jeol 1200 EX II electron microscope using a digital
1305 camera (Gatan).

1306 Low magnification EM images were overlaid and used to co-register the EM sections with the LM (Nissl)
1307 images, using vasculature and cell body (soma) landmarks. The Layer 4 region was determined by cyto-
1308 architecture, then drawn on the EM image.

1309 *Physical disector:* A regular sampling grid of 45 x 45 μm was generated within this layer 4 region, and
1310 high magnification images were taken at each of these sampling points for disector analysis. Reference
1311 and lookup section were separated by one intervening ultrathin section so that the disector 'z'
1312 dimension was 0.08 μm. Both sections were used as reference and as lookup in order to double the
1313 sample [66, 69]. Three hundred and forty one disectors were used from 3 mice. The disectors had a size
1314 of 5 × 5 μm and at 3.6 nm per pixel. Synapses and associated structures were classified using
1315 conventional criteria [70, 71]. The percentage of thalamic synapses was calculated by dividing the
1316 number of synapses formed by labeled boutons by the total number of asymmetric synapses (putative
1317 excitatory).

1318

1319 *Extracellular electrophysiological recordings in vivo*

1320 All electrophysiological recordings were performed in the left hemisphere of awake adult C57Bl/6 mice
1321 (2 to 6 months, males). A few weeks before the recordings, mice were first implanted with a metallic
1322 headplate using aseptic conditions and under anesthesia (see details in [6]). The day before or of
1323 recording, we performed a craniotomy over V1 (~0.5 x 0.5 mm above the monocular portion of V1, 2.5
1324 mm lateral to lambda) and implanted a reference skull screw; if the day before, then the exposed skull
1325 was sealed with Kwik Cast. On the day of recording the exposed cortex and skull were covered with 1%
1326 agarose in saline in order to prevent drying and to help maintaining mechanical stability.
1327 Dexamethasone was given to the animals to avoid brain inflammation (2 mg/kg, sc) and atropine to
1328 keep the respiratory tract clear (0.3 mg/kg, ip). Then, awake mice went into the recording setup. The
1329 headplate was clamped for stability, while the animal was free to run or remain still on a freely rotating
1330 disk. Multi-site silicon electrode arrays (imec Neuropixels) were dipped in DiI allowing post hoc
1331 visualization of the electrode path and lowered with a microdrive to a depth of 800-1000 μm. Reference
1332 and ground of the electrode were made through screws implanted in the skull. To improve the stability
1333 of recorded units, we allowed 20 minutes for the electrodes to settle.

1334 Neurophysiological signals were amplified, band-pass filtered, and acquired continuously at 20 or 30 kHz
1335 at 16-bit resolution using an Amplipex system (Amplipex Ltd) or Open Ephys system (open-ephys.org).
1336 The spike sorting procedure was described in detail previously [72]. In brief, algorithmic identification
1337 and unit assignment of spikes [73, 74] was followed by manual adjustment of the clusters [75, 76]. Only
1338 units with clear refractory periods and well-defined cluster boundaries were included in the analyses
1339 [73].

1340 Visual stimuli were largely the same as described above for simulations. The number of trials in the
1341 experiments was 50 for flashes, 10 for natural movies, and 100 for natural images. Rates of
1342 spontaneous activity were calculated by averaging the rates of each cell over 20 non-overlapping
1343 intervals, 500 ms long each, that were evenly distributed over 1 minute of continuous gray screen
1344 presentation (20 intervals of 500 ms were used for consistency with the 20 trials of gray screen
1345 presentation in simulations; see above). Moving bars were not used. Data for drifting gratings was
1346 taken from a previously published dataset [6].

1347 After the recording, mice were perfused and brains fixed, sectioned, and stained with DAPI (see details
1348 of histology and imaging in [6]) for reconstruction of the electrode path to assign a layer to each
1349 recording site.

1350 The laminar location of neurons was identified using histology and confirmed, when possible, by
1351 investigating the CSD depth profile of responses to full-field flashes. Putative excitatory neurons
1352 belonging to L4 according to this annotation were used for analysis. Since L4 is thin, and the fraction of
1353 inhibitory neurons is only ~15%, we could not obtain a sizeable number of such neurons for L4 in our
1354 recordings. Because of that, putative fast-spiking inhibitory neurons from all layers were combined for
1355 analysis.

1356

1357 *Whole-cell patch-clamp in vivo recordings*
1358
1359 Data of *in vivo* intracellular membrane potential (V_m) was obtained from genetically defined neuron
1360 populations in cortical layer 2/3 of mouse V1 via two-photon targeted whole-cell recordings. Adult (2 –
1361 4 months old, n = 2) transgenic mice expressing a red fluorescent cytosol marker tdTomato (tdT) under
1362 the control of the Cux2-CreERT2 promoter were used. Recordings were performed under Isoflurane (1–
1363 1.5% in O_2) anesthesia with ~7 MΩ glass micropipettes filled with K-Gluconate based internal solution
1364 (containing, in mM: potassium gluconate 125, NaCl 10, HEPES 20, Mg-ATP 3, Na-GTP 0.4, in ddH_2O; 290
1365 mOsm; pH 7.3; Alexa 488,50 µg/ml). Exposed V1 region was covered with Artificial Cerebrospinal Fluid
1366 (ACSF) containing (in mM: NaCl 126, KCl 2.5, NaH_2PO_4 1.25, $MgCl_2$ 1, $NaHCO_3$ 26, glucose 10, $CaCl_2$ 2, in
1367 ddH_2O; 290 mOsm; pH 7.3). tdT expressing neurons within 100 µm – 300 µm underneath the pia surface
1368 were targeted and patched, as described previously [77, 78, 79].

1369 Two-photon imaging was performed using a Sutter Moveable Objective Microscope (Sutter, CA USA)
1370 coupled with a tunable Ti:Sapphire femtosecond laser (Chameleon Ultra II, Coherent USA), controlled by
1371 the open-source software ScanImage 3.8 (Janelia Research Campus/ Vidrio Technologies), to visualize
1372 L2/3 neurons in V1. Neurons were imaged with a 40x water-immersion objective (LUMPLFLN 40XW,
1373 Olympus USA) at the excitation wavelength of 920 nm. Electrophysiology Signals were amplified with a
1374 Multiclamp 700B, digitized with a Digidata 1440B at 20kHz, using pClamp software (Molecular Devices)

1375 and stored on a PC (Dell, USA). Quality of the pipette was checked both electrically and optically. Pipette
1376 would be discarded if disproportional increase of pipette resistance (Rp) occurred, which indicates
1377 occlusion of pipette tip. Optically checked ejection of dye under two-photon imaging was also used to
1378 indicate whether the pipette was free of occlusion. If both the electrical and optical measures agreed
1379 the tip is clogged, the penetration would be terminated and the pipette was retracted and discarded.

1380 To conduct *in vivo* whole-cell recordings, clean pipette was manually advanced towards the target
1381 neuron with a low positive pressure (~20 mbar above ambient) under two-photon imaging with Rp
1382 constantly monitored. Pipette capacitance was compensated before patching the cell. Standard
1383 procedures were used to rapidly form a gigaseal [77, 78, 79]. After gigaseal formation, a brief negative
1384 pressure was used to rupture the membrane inside the tip to achieve the whole-cell configuration. V_m
1385 was recorded under current clamp mode with series resistance (Rseries) appropriately compensated.
1386 Spontaneous V_m activity was recorded for at least $1 - 2$ mins. The recordings were not corrected for
1387 liquid junction potential.

1388

1389 *Optogenetic manipulations and extracellular electrophysiological recordings in vivo*

1390 We performed in vivo multichannel silicon probe recordings from the primary visual cortex of mice as
1391 previously described [52]. Briefly, mice were anesthetized with a combination of 5 mg/kg
1392 chlorprothixene (intraperitoneal) and 1.2 g/kg urethane (intraperitoneal); during surgery mice were
1393 supplemented with 0.5-1.0% isoflurane. A head frame with an ~2 mm central opening was mounted
1394 over V1 and the skull was thinned using a dental drill. PBS was then applied to the thinned skull and
1395 sharpened forceps were then used to remove a small portion of skull wide enough to permit insertion of
1396 a NeuroNexus 32-channel linear probe (A1x32-Edge-5mm-20-177). The probe was inserted at a depth of
1397 800–1,000 µm. PBS was then applied to keep the craniotomy moist. Following a recovery period
1398 following probe insertion of at least 20 minutes, visual stimuli were presented using a gamma-corrected,
1399 Dell 52 3 32.5 cm LCD monitor (60 Hz refresh rate, mean luminance 50 cd/m2, 25 cm from contralateral
1400 eye). We used the Psychophysics Toolbox [80] to generate and present full-field sinusoidal drifting
1401 gratings (temporal frequency, 2 Hz; Spatial frequency, 0.04 cycles per degree; 2 orientations, 0 and 90
1402 degrees; contrasts 0, 10, 18, 32, 64, and 100% contrast). Drifting gratings were presented for 1500 ms
1403 and optogenetic stimulation trials were interleaved with non-optogenetic trials. Each trial was separated
1404 with 3-6 s inter-trial interval with a gray screen. To photostimulate archaerhodopsin (optogenetic trials)
1405 we used a 1 mm LED fiber with ~20 mW power output at the fiber tip, which was placed 0.5 mm from
1406 skull above recording location (590 nm, 1 mm diameter, Doric Lenses). The optogenetic light delivery
1407 lasted 1.9 s and started 200 ms prior to the visual stimulus and ended 200 ms following the stimulus.
1408 Black foil (Thor Labs) was shaped into a shield around LED and headframe in order to prevent the LED
1409 light from reaching the eyes. Recordings were amplified 1,000X and band-pass filtered between 0.3 Hz
1410 and 5 kHz using an AM systems 3500. Acquisition was done at 20 kHz with a NIDAQ PCIe-6239 board
1411 using custom MATLAB software (MathWorks).

1412 Data were analyzed with custom-written software using MATLAB. Single units were isolated using
1413 software provided by D.N. Hill, S.B. Mehta, and D. Kleinfeld [81]. Signals were high-pass filtered at 500
1414 Hz and waveforms were extracted from four adjacent electrode sites. Spikes were defined as events
1415 exceeding 4–5 SD of the noise. Waveforms were clustered using a k-means algorithm and further
1416 aligned using a graphical user interface. Fisher linear discriminant analysis and refractory period

46

1417   violations were used to assess unit isolation quality. Units were assigned a depth based on the channel
1418   in which they showed the strongest signal. In this work, only the data corresponding to drifting gratings
1419   with 100% contrast was used.

1420   The following mouse lines were used for in vivo extracellular recordings: Scnn1a-Tg3-Cre (stock number:
1421   009613; B6;C3-Tg(Scnn1a-cre)3Aibs/J) and Ai35(RCL-Arch/GFP) (stock number: 012735; B6;129S-
1422   Gt(ROSA)26Sortm35.1(CAG-aop3/GFP)Hze/J).

1423

1424   ***Data Analysis***

1425   Data analysis was performed on all simulations carried out for a given stimulus, as described in **Table S2**.
1426   That typically involved at least two independent models (usually three models) and multiple trials. Data
1427   from these multiple models and trials were typically combined together to produce summary plots.

1428   Summary figures that present box plots of various analyzed quantities adhere to the following standard.
1429   The box bottom and top represent the lower boundary of the second quartile of the data and the top
1430   boundary of the third quartile, respectively, thus marking the inter-quartile range (IQR); the median is
1431   shown in red. Whiskers mark +/-1.5 IQR from the bottom and top of the plot, as long as there are data
1432   points in that range. The rest of the data (outliers) are shown as separate dots or other symbols. In
1433   cases when the plot range does not include the whole span of the data (which was sometimes necessary
1434   due to the log-normal-like distribution of the data points over several orders of magnitude), the outliers
1435   outside of the plot range are not shown explicitly but are instead indicated by an arrow. The numbers
1436   next to such arrows ("N1/N2") indicate the number of such outliers that are not shown (N1) and the
1437   total number of data points (N2). The mean and s.e.m. of the data are shown on these plots as circles
1438   with error bars (thick black lines).

1439

1440   *Computation of the features of firing rate responses*

1441   Spontaneous activity was characterized by analyzing the responses of cells from 20 gray screen trials,
1442   each 1,000 ms long. For each cell, the spikes from the second 500 ms of every trial were used to
1443   compute the firing rate, which was then averaged over trials.

1444   The maximal response to gratings (R_{max}), the orientation selectivity index (OSI) and the direction
1445   selectivity index (DSI) were computed using responses to drifting gratings (disregarding the first 500 ms
1446   of the gray screen). First, the firing rate for each cell was obtained, using spikes from the 2,500 ms of
1447   grating presentation, and averaging over all trials. This rate was computed separately for every grating
1448   condition. The R_{max} metric for each cell was the maximal firing rate among all conditions.

1449   Following [6], we used the firing rate directly to compute the OSI and DSI (i.e., without subtracting the
1450   spontaneous rate). The analysis was performed for each cell independently. For each orientation, an
1451   average response across all SF and TF was computed, and the orientation that corresponded to the
1452   greatest averaged response was assigned as the preferred orientation of the cell. The SF and TF that
1453   evoked the strongest response at the preferred orientation were then considered as preferred
1454   frequencies. OSI and DSI were computed using the responses at all orientations for these preferred SF
1455   and TF. The OSI was computed as one minus the circular variance,

47

1456
$$OSI = \left| \frac{\sum_k f_k e^{2i\theta_k}}{\sum_k f_k} \right|,$$

1457 where k is the index for summation over all directions θ_k, and f_k is the firing rate response for each
1458 direction. The DSI was computed as

1459
$$DSI = \frac{f_{pref} - f_{null}}{f_{pref} + f_{null}},$$

1460 where f_{pref} is the firing rate response at the preferred direction (θ_{pref}) and f_{null} is the response at the
1461 opposite direction ($\theta_{pref} + \pi$).

1462 Responses to flashes were characterized by averaging firing rates of multiple cells in multiple trials, in 2
1463 ms bins. The number of trials was 10 for simulations and 50 for experiments. For simulations, the
1464 averaging was done separately for each of the two models for which 50 ms flash stimuli were simulated,
1465 and for each of the three biophysical excitatory cell populations, resulting in 6 firing rate vs. time traces.
1466 For experiments, the averaging was done separately for each mouse over all L4 excitatory cells, resulting
1467 in 8 traces. The peak magnitude and time to peak from the flash onset were then computed on each of
1468 those traces for the 1st and 2nd peaks.

1469

1470 *Spectra of the local field potential (LFP) and of spiking activity*

1471 The extracellular potential Φ was calculated along the central axis of the model (perpendicular to the L4
1472 plane), at locations distributed with the increments of 10 μm along the axis. The extracellular potential
1473 at the j-th location (i.e., electrode site) for a particular cell was computed as $\Phi_j = \sum_k R_{jk} I_k$, where I_k is
1474 the membrane current through the k-th neuronal compartment and R_{jk} is the transfer resistance
1475 between k-th neuronal compartment and the j-th electrode site. The transfer resistances were
1476 computed using the line-source approximation [82] assuming homogeneous and isotropic extracellular
1477 conductivity of 0.3 S/m. The contributions of the individual cells to the recordings are then summed up
1478 to find the total recorded potential at each recording electrode site. The membrane currents were
1479 obtained with NEURON's cvode.use_fast_imem() function which returns the transmembrane currents
1480 without needing to utilize the computationally expensive extracellular mechanism. The computation of
1481 the extracellular potential was implemented by modifying the NEURON's advance() function—called on
1482 each time step—to include the function call to our Python module computing the extracellular potential.

1483 The local field potential (LFP) was obtained by low-pass filtering the simulated extracellular potential
1484 with the 6th-order Butterworth filter, with the cutoff frequency of 200 Hz. The power spectra of the LFP
1485 (computed employing the fast Fourier transform) were then used for analysis of oscillations in
1486 population activity. The LFP recorded at the site closest to the center of the model was utilized for this
1487 analysis.

1488 Power spectra of spiking activity (**Fig. S6**) were computed as follows. A position in space was selected
1489 for recording; in all cases in this work we chose the center of the model for this purpose. The signal was
1490 then computed as the inverse-distance weighted multiunit activity, i.e., the time-binned firing rate
1491 accumulated from all neurons with the weight $1/r_i$, where r_i is the distance from the neuron's soma to

1492 the recording position. The time bin of 1 ms was used. The power spectrum was then computed using
1493 fast Fourier transform.

1494 Both LFP and spiking activity spectra were averaged over all trials of a given stimulus.

1495

1496 *Computation of sparsity*

1497 Sparsity of responses was computed following the definition in [50]. The formula used was

1498
$$S = \frac{1 - \frac{\left(\frac{\Sigma_i f_i}{n}\right)^2}{\frac{\Sigma_i f_i^2}{n}}}{1 - \frac{1}{n}},$$

1499 where S is the sparsity, f is the response (we used the firing rates averaged for each cell within each
1500 time bin over all trials for a given visual stimulus), and n is the number of samples i. The lifetime
1501 sparsity can be defined for each cell, and then samples i correspond to time bins distributed over the
1502 time axis, for a given visual stimulus.
1503
1504 For purposes of illustrating sparsity in our simulations, we computed lifetime sparsity for the three
1505 natural movies and three drifting grating stimuli (SF=0.05 cpd, TF=4 Hz, orientation of 0, 45, and 90
1506 degrees). Since gratings were presented for 2.5 seconds vs. 4.5 seconds for the movies, only the first 2.5
1507 seconds of movie responses were used for this analysis (to enable equal comparison).
1508
1509
1510 *Measurement of the excitatory currents in the model*

1511 To measure the currents flowing through the somata of biophysical cells, we used NEURON's function
1512 SEClamp(), which provides a simple voltage clamp. Out of all 10,000 biophysical cells in a model, every
1513 200th cell was voltage-clamped at the soma at -70 mV, to measure the excitatory current [7]. Thus, the
1514 currents were recorded for 50 cells in such a simulation (e.g., cell ID 2, 202, 402, 602, 802, …, 9802). The
1515 currents were saved from the SEClamp() objects, at each simulation time step.

1516 For the measured current, the F0 (mean) and F1 (amplitude at the frequency of the stimulus)
1517 components were obtained according to Ref. [7]. The current was averaged over trials and then cycle-
1518 averaged. F0 was computed as the mean (over the cycle time) of the cycle-averaged current. F0 was
1519 then subtracted from the cycle-averaged current, and the result was fit with a sinusoid function at the
1520 stimulus frequency, $b\sin(\omega t + \varphi)$, where $\omega = 2\pi\nu$ (ν being the stimulus frequency). The F1
1521 component value was taken as $F_1 = 2|b|$.

1522 For all-LIF models, we measured contribution of LGN synaptic inputs to the total excitatory synaptic
1523 inputs as a proxy to the excitatory synaptic currents measured for the biophysical model. Specifically,
1524 for each spike arriving to a synapse, that synapse contributed its weight to the accumulating sum for the
1525 target cell; the sum was computed for synapses from LGN only or for all synapses and was normalized by
1526 time and number of trials.

1527
1528
1529

1530

Methods References

1532 [54] Richardson, R.J., Blundon, J.A., Bayazitov, I.T., and Zakharenko, S.S. Connectivity Patterns Revealed
1533 by Mapping of Active Inputs on Dendrites of Thalamorecipient Neurons in the Auditory Cortex. *J. Neurosci.* **29**, 6406–6417 (2009).

1535 [55] Schoonover, C.E. Comparative Strength and Dendritic Organization of Thalamocortical and
1536 Corticocortical Synapses onto Excitatory Layer 4 Neurons. *J. Neurosci.* **34**, 6746–6758 (2014).

1537 [56] da Costa, N. and Martin, K.A.C. How Thalamus Connects to Spiny Stellate Cells in the Cat's Visual
1538 Cortex. *J. Neurosci.* **31**, 2925–2937 (2011).

1539 [57] Douglas, R.J., and Martin, K.A.C. Inhibition in cortical circuits. *Current Biology* **19**, R398–R402
1540 (2009).

1541 [58] Spruston, N. Pyramidal neurons: dendritic structure and synaptic integration. *Nat. Rev. Neurosci.* **9**,
1542 206-221 (2008).

1543 [59] Pfeffer, C.K., et al. Inhibition of inhibition in visual cortex: the logic of connections between
1544 molecularly distinct interneurons. *Nature Neurosci.* **16**, 1068-1076 (2013).

1545 [60] Beierlein, M., Gibson, J.R., and Connors, B.W. Two Dynamically Distinct Inhibitory Networks in
1546 Layer 4 of the Neocortex. *J. Neurophys.* **90**, 2987-3000 (2003).

1547 [61] Niell, C.M., Bonin, V., and Andermann, M.L. Functional Organization of Circuits in Rodent Primary
1548 Visual Cortex. In *The New Visual Neurosciences*, Werner, J.S.and Chalupa, L.M., Eds. MIT Press (2013).

1549 [62] Liu, B. et al. Visual Receptive Field Structure of Cortical Inhibitory Neurons Revealed by Two-Photon
1550 Imaging Guided Recording. *J. Neurosci.* **29**, 10520 – 10532 (2009).

1551 [63] Welles, O. Touch of Evil (United States: Universal - International). (1958).

1552 [64] Martin, D., Fowlkes, C., Tal, D., and Malik, J. A database of human segmented natural images and
1553 its application to evaluating segmentation algorithms and measuring ecological statistics. *Proc. Eighth
1554 IEEE Int. Conf. Comput. Vision. ICCV 2001* **2**, 416 – 423 (2001).

1555 [65] van Hateren, J.H., and van der Schaaf, A. Independent component filters of natural images
1556 compared with simple cells in primary visual cortex. *Proc. Biol. Sci.* **265**, 359 – 366 (1998).

1557 [66] da Costa, N. M., Hepp, K., & Martin, K. A. C. A systematic random sampling scheme optimized to
1558 detect the proportion of rare synapses in the neuropil. *Journal of Neuroscience Methods*, **180**, 77–81.
1559 (2009).

1560 [67] Sterio, D. The unbiased estimation of number and sizes of arbitrary particles using the disector. *J
1561 Microsc*, **134** (Pt 2), 127–136 (1984).

1562

1563 [68] Coleman, J.E., et al. Rapid Structural Remodeling of Thalamocortical Synapses Parallels Experience-
1564 Dependent Functional Plasticity in Mouse Primary Visual Cortex. *J. Neurosci.* **30**, 9670-9682 (2010).

[69] Howard, C., and Reed, M. Unbiased stereology (2nd ed.). New York. (2005).

[70] Gray, E. G. Electron microscopy of synaptic contacts on dendrite spines of the cerebral cortex. **183**, 1592–1593 (1959).

[71] Colonnier, M. Synaptic patterns on different cell types in the different laminae of the cat visual cortex. An electron microscope study. *Brain Research*, *9*, 268–287 (1968).

[72] Mizuseki K, Sirota A, Pastalkova E, Buzsaki G. Theta oscillations provide temporal windows for local circuit computation in the entorhinalhippocampal loop. *Neuron* **64**, 267–280 (2009).

[73] Harris KD, Henze DA, Csicsvari J, Hirase H, Buzsaki G. Accuracy of tetrode spike separation as determined by simultaneous intracellular and extracellular measurements. *J Neurophysiol* **84**, 401–414 (2000).

[74] Pachitariu M, Steinmetz NA, Kadir S, Carandini M and Harris KD. Kilosort: realtime spike-sorting for extracellular electrophysiology with hundreds of channels. *bioRxiv* dx.doi.org/10.1101/061481 (2016).

[75] Hazan L, Zugaro M, Buzsaki G. Klusters, NeuroScope, NDManager: a free software suite for neurophysiological data processing and visualization. *J Neurosci Methods* **155**, 207–216 (2006).

[76] Rossant, C. et al. Spike sorting for large, dense electrode arrays. *Nat. Neurosci.* **19**, 634–641 (2016).

[77] Kitamura K, Judkewitz B, Kano M, Denk W, Häusser M. Targeted patch-clamp recordings and single-cell electroporation of unlabeled neurons in vivo. *Nat Methods* **5**, 61-67 (2008).

[78] Judkewitz B, Rizzi M, Kitamura K, Häusser M. Targeted single-cell electroporation of mammalian neurons in vivo. *Nat Protoc.* **4**, 862-869 (2009).

[79] Long B, Li L, Knoblich U, Zeng H, Peng H. 3D Image-Guided Automatic Pipette Positioning for Single Cell Experiments in vivo. *Sci Rep.* **5**, 18426 (2015).

[80] Brainard, D.H. The Psychophysics Toolbox. *Spat Vis.* **10**, 433-436 (1997).

[81] Fee, M.S., Mitra, P.P., Kleinfeld, D. Automatic sorting of multiple unit neuronal signals in the presence of anisotropic and non-Gaussian variability. *J. Neurosci. Meth.*, **69**, 175-188 (1996).

[82] Holt, G.R., and Koch, C. Electrical interactions via the extracellular potential near cell bodies. *J Comput Neurosci.* **6**, 169-184 (1999).